Antagonistic inhibitory subnetworks control cooperation and competition across cortical space

Daniel P. Mossing[1,2], Julia Veit[2,3], Agostina Palmigiano[4], Kenneth D. Miller[4,5] and Hillel Adesnik[2,6]
[1]Biophysics Graduate Group, University of California, Berkeley
[2]Dept. of Molecular and Cell Biology, University of California, Berkeley
[3]Present address: Institute of Physiology I, University of Freiburg
[4]Center for Theoretical Neuroscience, College of Physicians and Surgeons and Mortimer B. Zuckerman Mind Brain Behavior Institute, Columbia University
[5]Dept. of Neuroscience, Swartz Program in Theoretical Neuroscience, Kavli Institute for Brain Science, College of Physicians and Surgeons and Mortimer B. Zuckerman Mind Brain Behavior Institute, Columbia University
[6]The Helen Wills Neuroscience Institute, University of California, Berkeley

Abstract

The cortical microcircuit can dynamically adjust to dramatic changes in the strength, scale, and complexity of its input. In the primary visual cortex (V1), pyramidal cells (PCs) integrate widely across space when signals are weak, but integrate narrowly when signals are strong, a phenomenon known as contrast-dependent surround suppression. Theoretical work has proposed that local interneurons could mediate a shift from cooperation to competition of PCs across cortical space, underlying this computation. We combine calcium imaging and electrophysiology to constrain a stabilized superlinear network model that explains how the four principal cell types in layer 2/3 (L2/3) of mouse V1– somatostatin (SST), parvalbumin (PV), and vasoactive intestinal peptide (VIP) interneurons, and PCs transform inputs from layer 4 (L4) PCs to encode drifting gratings of varying size and contrast. Using bidirectional optogenetic perturbations, we confirm key predictions of the model. Our data and modeling show that network nonlinearities set up by recurrent amplification mediate a shift from a positive PC-VIP feedback loop at small size and low contrast to a negative PC-SST feedback loop at large size and high contrast to support this flexible computation. This may represent a widespread mechanism for gating competition across cortical space to optimally meet task demands.

Introduction

The brain must process sensory inputs across a wide range of sensory environments and perceptual goals. When sensory signals are weak, adding of activity in ensembles encoding congruent evidence across space ("corroboration") could optimize detection; when signals are strong, subtraction of congruent signals ("explaining away") could optimize discrimination or localization (Sceniak, et al. 1999, Hawken, et al. 2001, Nauhaus, et al. 2009). For a sensory code to capture this flexible functional interaction, neural ensembles encoding distinct elements of sensory evidence must be able to rapidly change the nature of their interaction, competing or cooperating depending on sensory inputs.

Causal and correlative evidence suggests that with increasing contrast, interactions across cortical space become less cooperative and more competitive (Nauhaus, et al. 2009,

Sato, Häusser and Carandini 2014). However, the network mechanisms underlying this shift are incompletely understood. Theoretical work has proposed that local inhibition mediates the transition from cooperative to competitive spatial interactions (Angelucci et al., 2017; Schwabe et al., 2010); yet whether distinct interneuron subtypes play dissociable roles is unknown (Rubin et al., 2015). In this study, we determine how a cortical microcircuit of genetically defined interneuron subtypes underlies this shift from cooperation to competition across cortical space.

Three interneuron subtypes, parvalbumin- (PV), somatostatin- (SST) and vasoactive intestinal peptide- (VIP) expressing, comprise 80-85% of cortical interneurons. All three subtypes have been found to shape the sensory coding properties of pyramidal cells, the primary output neurons of cortex, in distinct ways to facilitate cortical encoding of sensory features (Adesnik et al., 2012; Ayzenshtat et al., 2016; Lee et al., 2012; Rudy et al., 2011; Wilson et al., 2012). VIP cells specialize in inhibition of other interneurons (Pi, et al. 2013, Lee, et al. 2013, Pfeffer, et al. 2013) and may thus play a crucial role in gating cortical competition. VIP cells receive feedback excitation from higher areas (Zhang, et al. 2014) and strong neuromodulatory input from the midbrain (Fu, et al. 2014) which positions them to mediate top-down control of flexible functional interactions in the cortex (Wang & Yang, 2018; Yang et al., 2016). Recent work has shown that VIP cells, like PCs and PV cells, are highly surround suppressed (Dipoppa et al., 2018), are sensitive to low contrasts (Millman et al., 2019), and prefer spatially heterogeneous as opposed to homogeneous textures (Keller, Roth, Caudill, et al., 2020). Because VIP cells preferentially innervate SST cells (Pfeffer et al., 2013), which are known to control spatial summation in the cortex (Adesnik, et al. 2012), we hypothesized a novel role for VIP cells, in contributing to the contrast dependence of cooperation and competition across cortical space.

Because cortical neurons' firing rate depends superlinearly on their input current (Anderson, et al. 2000, Miller and Troyer 2002), effective monosynaptic connection strength depends on the activity level of the postsynaptic neuron. A relatively inactive neuron, whose average membrane potential is far from its spike threshold, is insensitive to changes in its input. On the other hand, a highly active neuron, depolarized close to action potential threshold, will sensitively transduce changes in its synaptic inputs to changes in its spike rate. Because postsynaptic neurons' activity is tuned to stimulus features, effective monosynaptic connection strength can itself show stimulus tuning. Because polysynaptic effects depend on the activity of all intervening cell types, the stimulus tuning of total functional connectivity can be combinatorially complex. Tuned functional connectivity via polysynaptic effects in a superlinear network could represent a computationally powerful mechanism for shaping interactions between ensembles encoding distinct features of the sensory environment (Ahmadian et al., 2013; Del Molino et al., 2017; Rubin et al., 2015).

We hypothesized that cortical VIP-SST inhibitory microcircuitry in combination with cell-intrinsic firing rate nonlinearities underlies contrast dependent surround suppression. We combined experiment and theory to test whether firing rate nonlinearities dynamically set effective monosynaptic connection strengths, and via polysynaptic effects the total functional connectivity, between the four principal cortical subtypes to flexibly support cooperation or competition of PCs across space. To achieve this, we first recorded from the major cell types of the upper cortical layers in V1 with two photon imaging and electrophysiology while stimulating

V1 with drifting gratings of varying size and contrast. We then used these comprehensive observational data to fit a circuit model that could explain contrast-dependent shifts from cooperation to competition across space in terms of shifting effective connection strength between genetically defined populations of neurons with superlinear responses to input current. Finally, we tested core predictions of this model with targeted optogenetic perturbations of VIP cells while measuring the impact on all other cell types. The insight that superlinearity *per se* could powerfully shape network responses was critical to interpreting optogenetic effects: at steep points in their superlinearities, neurons were more sensitive to perturbations. Residual effects, those not explained by activity level in the unperturbed condition, sensitively reflected the underlying functional connectivity of the network.

We find that VIP and SST activity outline contrasting regimes of sensory coding in PCs. In the VIP-dominated regime, when the network is weakly activated by stimuli of low contrast and small size, increasing PC activity drives VIP cells, which in turn disinhibit PCs, closing a positive PC-VIP feedback loop. PCs show surround facilitation and are highly sensitive to changes in contrast. Conversely, in the SST-dominated regime, when the network is strongly activated by stimuli of high contrast and large size, increasing PC activity instead drives SST cells, which in turn inhibit PCs, closing a negative feedback loop. PCs show surround suppression and are weakly sensitive to changes in contrast. Thus, the VIP-dominated regime optimizes the dynamic range of contrast encoding at the expense of the coding of space, while the SST-dominated regime optimizes dynamic range of size encoding at the expense of the coding of contrast. Our model explains that high spontaneous drive to VIP cells competes with spatially broad PC→SST drive to establish these disparate regimes of cortical operation. With increasing size and contrast, positive PC-VIP feedback, promoting cooperation of PCs across space, is gradually replaced by negative PC-SST feedback, promoting competition across space. We test key predictions of this model by showing that optogenetically enhancing the spontaneous drive to VIP cells powerfully drives activity in the positive feedback-dominated small and low contrast regime, and more weakly in the negative feedback-dominated large and high contrast regime. Finally, we show that contrast-dependent recurrent amplification within the PC-PV subnetwork enhances the difference between these two regimes of circuit operation. This work provides a detailed explanation for flexible cooperation and competition across cortical space by virtue of cortical microcircuitry and the intrinsic superlinearity of neurons. Furthermore, it establishes a generalizable approach for predicting and explaining how physiological or optogenetic perturbations propagate through a highly recurrent network.

Results

Cell-type specific encoding of size and contrast in the mouse primary visual cortex

To study a paradigmatic example of flexible cooperation and competition across cortical space, we first probed the logic of contrast-dependent surround suppression in layer 2/3 pyramidal cells (L2/3 PCs) of the primary visual cortex (V1). We recorded neural activity in awake, head-fixed mice (fig. 1a) using cell type-specific calcium imaging (fig. 1b). After mapping each neuron's receptive field, we independently varied the size, contrast, and direction of drifting gratings while keeping their location constant. We measured responses using deconvolved

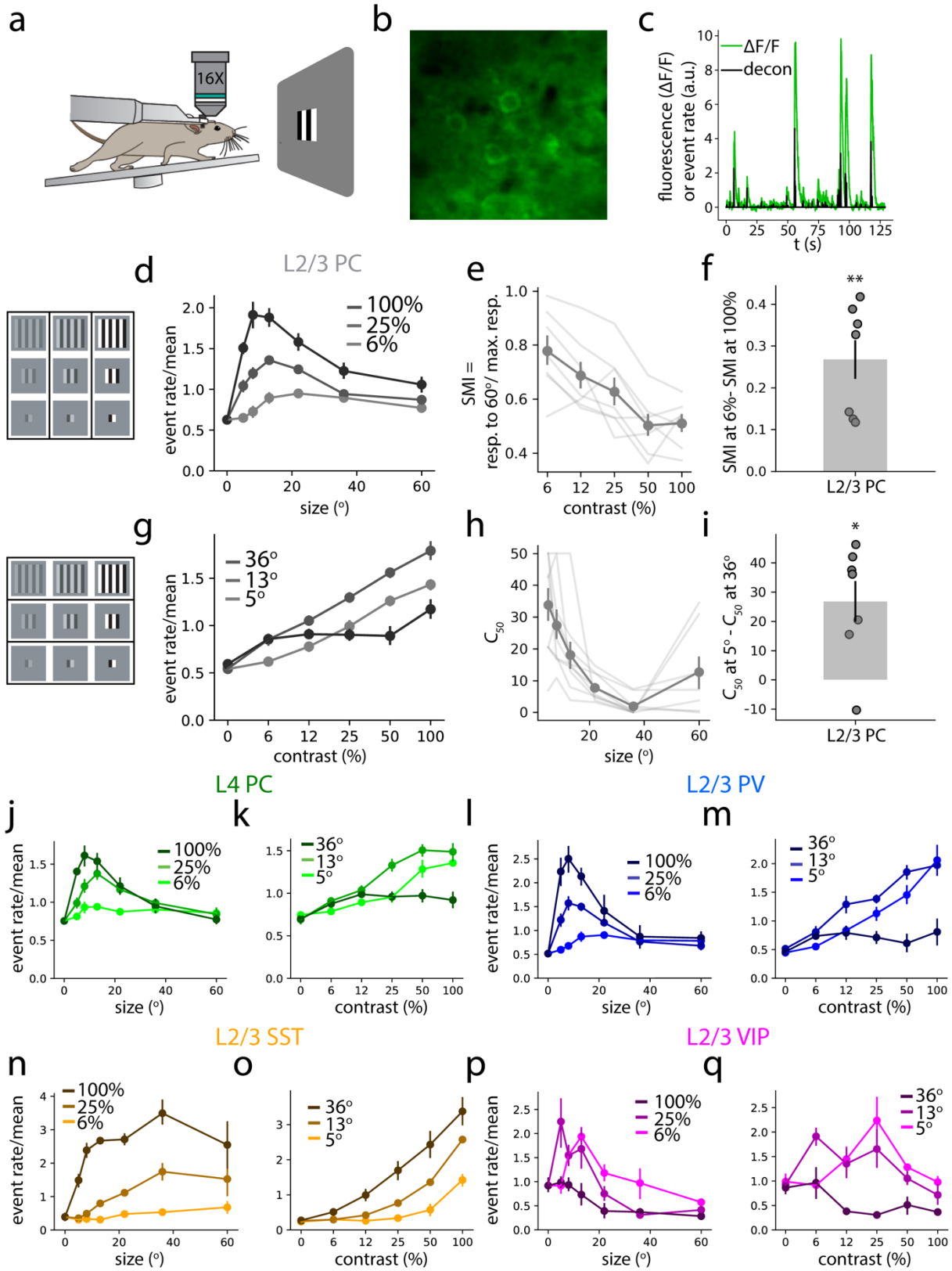
a
16X
b
c
ΔF/F
decon
fluorescence (ΔF/F) or event rate (a.u.)
t (s)
d
L2/3 PC
100%
25%
6%
event rate/mean
size (°)
e
SMI = resp. to 60°/ max. resp.
contrast (%)
f
**
SMI at 6%- SMI at 100%
L2/3 PC
g
36°
13°
5°
event rate/mean
contrast (%)
h
C_{50}
size (°)
i
*
C_{50} at 5° - C_{50} at 36°
L2/3 PC
L4 PC
j
k
L2/3 PV
l
m
L2/3 SST
n
o
L2/3 VIP
p
q

Figure 1. Cell type-specific responses to stimulus size and contrast in mouse V1. A) Mice were head-fixed and free to run on a circular treadmill, while passively viewing a monitor showing drifting gratings of varying size, contrast, and direction. B) Transgenic mouse lines were used to express gCaMP6s in defined subsets of neurons. C) Event rate deconvolved from gCaMP fluorescence was used to estimate neural activity. D) Averaged deconvolved event rates in L2/3 PCs are plotted against drifting grating patch size, with different contrasts plotted separately. Event rates are normalized to the mean across all stimuli and all neurons within each imaging session. In all size tuning plots, darker color corresponds to higher contrast. E) Surround modulation index (SMI) is defined as the response to 60° gratings divided by the response to the preferred size for each contrast. Each transparent line corresponds to an imaging session, and the solid line corresponds to the average across sessions. F) To quantify the contrast dependence of surround suppression, the SMI at the lowest contrast (6%) is subtracted from the SMI at the highest contrast (100%). This difference of SMI corresponds to the magnitude of contrast dependence of surround suppression. G) The same tuning curves as in D) are plotted, separated by size, with contrast varying along the x-axis. In all contrast tuning plots, darker color corresponds to larger size. H) Naka-Rushton functions were fit to contrast tuning curves for each L2/3 PC experiment. Plotted is C_{50}, the contrast evoking a half-maximal response for the fit Naka-Rushton function, as a function of size, for each experiment (transparent lines) and averaged (bold lines). I) As a global metric of size-dependent contrast sensitivity, we compute the difference in C_{50} between the 5° and 36° size. J-Q) Same as D), G), for L4 PCs, L2/3 PV cells, L2/3 SST cells, and L2/3 VIP cells, respectively. ** significantly different from zero, $p < 0.01$, Wilcoxon signed rank test. Error bars represent bootstrap SEM equivalent.

event rate (fig. 1c, see Methods), and first restricted our analysis to neurons within 10 degrees of retinotopic space of the center of the stimulus representation, and trials on which the animal was not locomoting (see Methods). To specifically examine tuning for size and contrast, we averaged responses across the directions sampled. We first asked how size tuning varied as a function of contrast. Prior electrical recordings from unidentified cell types in monkeys (Cavanaugh et al., 2002; Kapadia et al., 1999; Levitt & Lund, 1997; Sceniak et al., 1999), cats (Polat et al., 1998; Sengpiel et al., 1997; Toth et al., 1996), and mice (Ayaz et al., 2013; Nienborg et al., 2013; Vaiceliunaite et al., 2013) have established that surround suppression in V1 increases with increasing contrast. Consistent with these findings, we found that at high contrast, L2/3 PC responses showed strong bandpass size tuning, peaking sharply at small sizes, while at low contrast, responses peaked more broadly, and at larger size (fig. 1d). Because stimuli of increasing size drive activity in distal (surrounding) regions of cortical space, this is consistent with a picture in which surround PCs cooperate with center PCs at low contrast (supporting broad size tuning) and compete with center PCs at high contrast (supporting sharp tuning for small sizes).

In order to quantify the degree of surround suppression as a function of contrast, we computed a surround modulation index (SMI) defined as the response to 60° gratings (the largest shown) at a given contrast, divided by the response to the preferred size at the same contrast. We computed these metrics on the population-averaged tuning curves for each imaging session. SMI decreased monotonically, corresponding to strengthening surround suppression, with increasing contrast (fig. 1e). As a global metric for the contrast dependence of surround suppression, we computed the difference of SMI at 6% contrast and 100% contrast. We found that this difference was significantly positive (fig. 1f—Wilcoxon signed rank test, $p<0.05$), indicating that surround suppression increased in strength with increasing contrast.

Enhanced surround facilitation at low contrast has been theorized to enhance detectability of large textures. If this were the case, we would expect to see sensitivity to low contrast stimuli increase with size. We measured this change in sensitivity directly by taking a complementary view of the same data, examining contrast tuning at each size (fig. 1g). The C_{50}, or contrast evoking half-maximal response, increased monotonically with size up to 36° (fig. 1h). As a global metric for the size dependence of contrast sensitivity, we computed the difference in C_{50} between 5° and 60° size; this difference was significantly positive (fig. 1i—Wilcoxon signed rank test, $p<0.05$). Thus, contrast sensitivity was enhanced at large sizes, consistent with spatial integration enhancing stimulus detectability.

We next asked whether these properties were robust across behavioral states and recording modalities. We found qualitatively similar results between the locomoting and non-locomoting conditions (fig. S1). To validate these measurements with electrical recordings, we performed analogous experiments in which we sampled V1 activity using multi-electrode arrays rather than calcium imaging. Regular spiking (RS) units could be compared with PCs in our calcium imaging data. Importantly, tuning measured with electrophysiology and calcium imaging closely agreed (fig. S2; non-locomoting, RS units, $R=0.82$, $p=2x10^{-8}$, Wald test).

To address the network mechanisms that might contribute to PC size and contrast tuning, we next probed the tuning of other cell types in the circuit. First, we asked whether similar tuning properties were present in the primary input layer of cortex, layer 4 (L4). Indeed, L4 PCs on average showed similar tuning (fig. 1j,k), suggesting tuning of feedforward inputs

contributes to contrast-dependent surround suppression. We then examined the principal inhibitory inputs to L2/3 PCs, local interneurons. Prior theoretical studies have proposed that local interneurons could support a contrast-adaptive code in PCs; one specific model predicts the existence of an inhibitory cell type that is selectively driven at high contrasts, driving surround suppression only under these conditions (Angelucci, et al. 2017). We first asked whether L2/3 PV cells, which share inputs with and strongly inhibit L2/3 PCs, might show enhanced selectivity for high contrast relative to L2/3 PCs. However, we found that in keeping with their high degree of shared inputs, tuning of PV cells closely matched that of PCs (fig. 1l,m). Fast spiking (FS) units measured using extracellular electrophysiology closely agreed with PV cell measurements (fig. S2; non-locomoting, FS units, R=0.84, $p=7x10^{-9}$, Wald test).

Therefore, we next examined a second major L2/3 interneuron subtype, SST cells. Previous work has implicated SST cells in contributing to surround suppression of PCs at high contrast (Adesnik, et al. 2012, Nienborg, et al. 2013). Although SST cells are known to prefer larger sizes than the other cortical cell types, how this depends on stimulus contrast is not known. In fact, SST tuning diverged sharply from that of PCs and PV cells. SST cells responded best at large size and high contrast, and weakly or not at all at small size and low contrast (fig. 1n). Examining SST contrast tuning at varying size showed that at small size, they were insensitive to all but the highest contrast; stimuli that drove nearly maximal activity in PCs and PV cells only weakly drove SST cells (fig. 1o). Since SST cells receive strong excitation from L2/3 PCs (Adesnik, et al. 2012, Hakim, Shamardani and Adesnik 2018, Kapfer, et al. 2007, Karnani, et al. 2016), this difference in tuning was surprising.

This raised the possibility that strong inhibition from L2/3 VIP cells to SST cells counteracts PC→SST excitation to explain SST cells' remarkable insensitivity to contrast. If this were true, VIP cells might show size and contrast tuning opposite to that of SST cells. VIP cells, which powerfully and preferentially inhibit SST cells (Pfeffer et al., 2013), exhibit the strongest surround suppression of all cell types at high contrast (Dipoppa, et al. 2018), and are highly sensitive to contrast at large size (Millman et al., 2019). Whether and how VIP contrast responses vary as a function of stimulus size, however, is not known. In line with our prediction, as a population VIP cells were selectively responsive at small size and low contrast, and strongly suppressed at large size and high contrast (fig. 1p; at a single neuron level, this population average reflected a mixture of behaviors, from strict contrast suppression, to bandpass size and contrast tuning (fig. S3)). Examining the same data as contrast tuning at varying size showed further stark differences between SST and VIP cells. Unlike SST cells' monotonic contrast tuning, VIP cells on average showed bandpass contrast tuning, with the preferred contrast decreasing with increasing size (fig. 1q). These data demonstrated that SST and VIP cells differentially encode stimulus size and contrast, and demarcate disparate regimes of visually-evoked inhibitory circuit activity – one in which VIP is active but SST is largely silent, and one in which SST is active and VIP activity is strongly suppressed. Thus, average VIP and SST responses were strongly anti-correlated across sizes and contrasts (fig. S4a, $p=5x10^{-5}$, Wald test).

Next, we asked how SST and VIP activity might relate to functional interactions of PCs across space. To address this, we first computed a local metric for PC spatial integration at each size and contrast: the slope of PC size tuning curves (fig. S4b). This metric was positive where PC responses were increasing with increasing size (surround facilitating), and negative where PC responses were decreasing with increasing size (surround suppressing). We then plotted this

metric against the difference between SST and VIP activity (which we termed the SST – VIP axis) for each stimulus condition. Indeed, we found that surround facilitation was strongly anti-correlated with movement along the SST – VIP axis (fig. S4c, R=-0.36, p=0.03, Wald test). We next asked whether the slope of PC contrast responses could likewise be explained by the differential activity of VIP and SST cells; as a metric for contrast sensitivity, we measured the local slope of PC contrast responses in a similar way (fig. S4d). Indeed, movement along the SST – VIP axis was strongly anti-correlated with PC contrast tuning slope (fig. S4e, R=0.44, $p=7\times10^{-3}$). Thus, in the VIP-dominated regime, PCs sensitively encoded contrast, and in the SST-dominated regime, PCs sensitively encoded spatial features.

A recurrent network model explains size and contrast tuning of the four cell-type circuit

The data presented above show that VIP and SST activity demarcate disparate regimes of inhibitory circuit operation in V1 L2/3. To understand mechanistically how these regimes might arise, and how they could give rise to contrast-dependent cooperation and competition of PCs across space, we developed a data-driven recurrent network model. The goal of this model was to explain how feedforward drive from L4, recurrent connectivity, and cell-intrinsic superlinearities interact to dynamically shift PC functional connectivity across space from cooperative to competitive with increasing stimulus size and contrast.

Using the comprehensive physiological data presented above, along with the responses of neurons of each cell type located in the surround of the stimulus representation (fig. S5), we fit a superlinear stabilized network model (see Methods). This model simulated two spatial domains (center and surround) each containing five cell types (fig. 2a): L4 PCs, which serve as feedforward inputs, and the four L2/3 cell types. In the model, each L2/3 cell type received a linear combination of inputs from each other population, transformed through a static nonlinearity to determine its firing rate (Miller and Troyer 2002) whose dynamics were described by:

$$\frac{d\boldsymbol{r}}{dt} = -\boldsymbol{r} + f(W\boldsymbol{r} + \boldsymbol{h}). \quad (1)$$

Here, $\boldsymbol{r}$ is a vector representing the firing rate of each cell type, W is the matrix of synaptic connection strengths, $\boldsymbol{h}$ is a vector of external inputs and bias currents, and f represents the static nonlinearity. Importantly, the network was constrained to be in an inhibitory stabilized regime across all stimulus conditions (Sanzeni et al., 2020). Importantly, many model fits were able to recapitulate key tuning features for each cell type (fig. 2b), including the contrast dependence of surround suppression of PCs and PV cells, the low contrast sensitivity and high size sensitivity of SST cells, and bandpass contrast tuning of VIP cells. We next analyzed the behavior of the best fitting models, starting from randomly initialized model parameters (see Methods) to identify robust features of network parameters explaining the calcium imaging data. The synaptic weight matrix averaged across successful model fits is presented in fig. 2b. Notably, many of the connection weights in these fits correspond well to known connections from prior studies, including the strong connections among PCs and PV cells, and the strong reciprocal inhibition between SST cells and VIP cells (Pfeffer et al., 2013). Distributions of model parameters across successful model fits are shown in fig. S6.

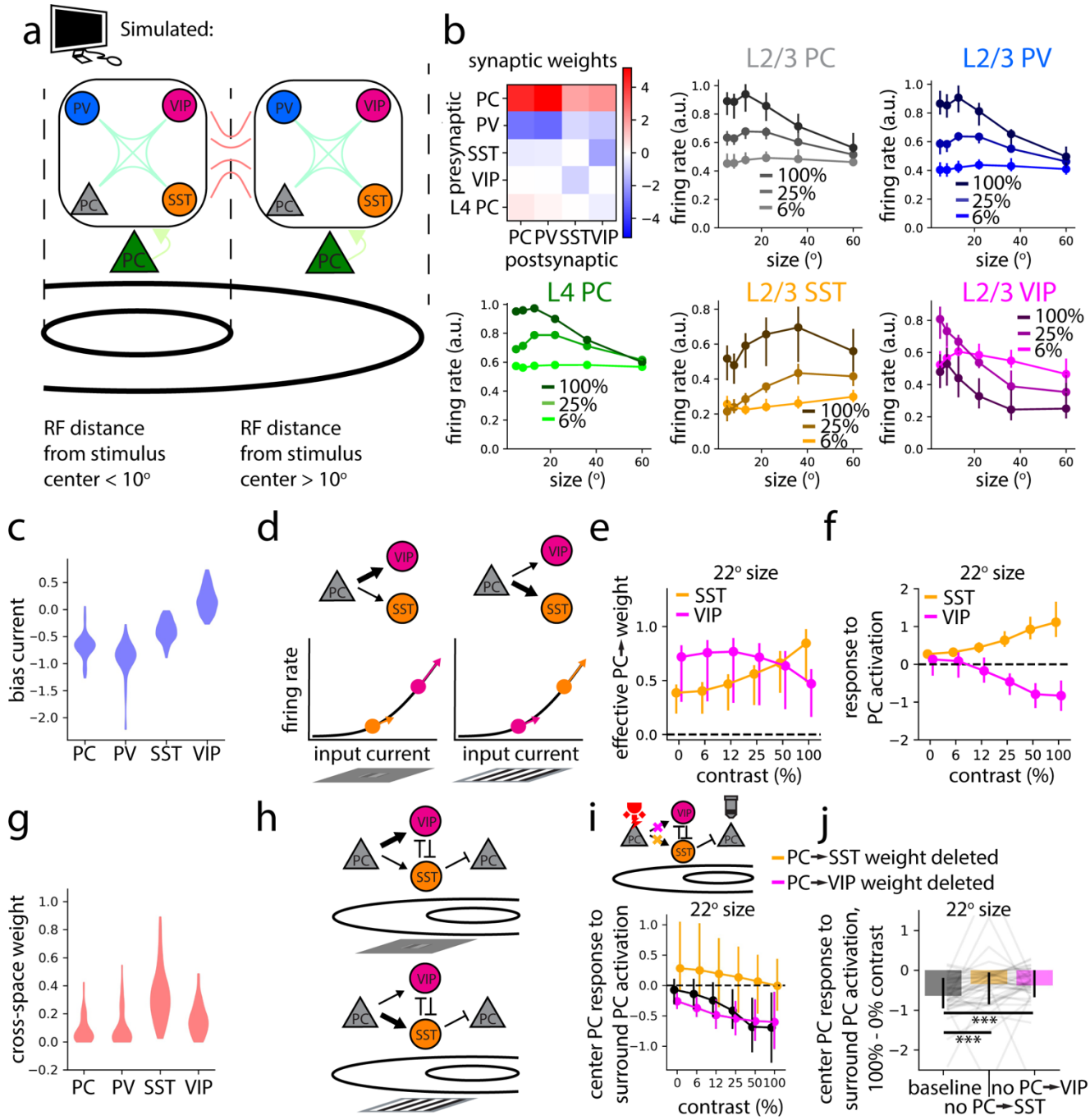

Figure 2. A network model explains tuning properties of layer 2/3 cell types. A) The rate-based network model consisted of five cell types, spread across two spatial domains. Using gradient descent on a loss function defined based on the calcium imaging data, we optimized a set of weights describing connection strengths among these cell types. Connections between two cell types across spatial domains were attenuated by a cross-space weight that was allowed to vary based on the postsynaptic cell type. B) Synaptic weight matrix between cell types averaged across model fits, and size tuning of all five modeled cell types, by contrast. C) Violin plots of bias currents to each cell type. D) Schematic depicting stimulus-dependent effective connections between PCs, and SST and VIP cells. Effective connection strengths are given by the

product of synaptic weight and firing rate nonlinearity slope. For small and low contrast stimuli, VIP cells sit at a steep point in their firing rate nonlinearity, and SST cells at a shallow point. Thus, effective PC→VIP connection strength is stronger than PC→SST. At large size and high contrast, the opposite is true. E) Effective connection strength between PC and SSTs (orange) or VIP (magenta) is plotted as a function of contrast, at 22° size, F) Modeled responses of SST or VIP to weak activation of PCs in both layers and spatial pixels are plotted as a function of contrast, at 22° size. G) Violin plots of cross-space weights for each cell type. H) Schematic depicting stimulus-dependent cooperation and competition between PCs across space. At small size and low contrast, surround PCs more effectively drive VIP cells, disinhibiting center PCs by inhibiting SST cells. At large size and high contrast, surround PCs more effectively drive SST cells, inhibiting center PCs. I) Top: schematic of the modeled perturbations, eliminating either PC→SST or PC→VIP connections. Bottom: Modeled responses of center PCs to weak activation of surround PCs are plotted as a function of contrast, at 22° size. Orange: same but deleting the PC→SST connection. Magenta: deleting the PC→VIP connection. J) The difference between center PC responses to surround PC activation at 100% contrast, and 0% contrast, at 22° size, for the intact network, and after deleting the PC→SST and PC→VIP connections. In the intact network, the difference is significantly larger across successful model fits ($p < 10^{-3}$, $p < 10^{-6}$, Wilcoxon signed-rank test). Error bars represent 16th to 84th percentile of model fits.

Our first goal was to understand the opposing contrast sensitivity of VIP and SST cells. Starting from spontaneous (0° size, or 0% contrast) activity, increasing PC activity seemed to first drive VIP activity and not SST activity, at small size and low contrast, and subsequently to suppress VIP activity while driving SST activity, at large size and high contrast. We first asked how a single set of synaptic weights could support these seemingly opposite effects depending on stimulus. We reasoned that a key ingredient might be the superlinear increase of firing rate with increasing input current. With this superlinearity, active neural populations would be sensitive to subsequent changes in their input, while inactive populations would be insensitive. Thus, the importance of a given connection in shaping network activity would increase with the activity level of the postsynaptic cell type.

First, we asked why at small size and low contrast, increasing PC activity drove VIP cells but not SST cells. We reasoned that high spontaneous drive to VIP cells could play a role. If spontaneous drive to VIP ("bias current" in the model) outweighed spontaneous drive to SST, then the slope of the VIP firing rate nonlinearity should be steep for low levels of sensory activity, while the slope of the SST firing rate nonlinearity should be shallow. Thus initially, starting from spontaneous activity, increasing PC activity could robustly drive VIP cells, but not SST cells. Consistent with this notion, in our physiological data VIP cells exhibited nearly half maximal activity during spontaneous activity, while SST cells exhibited only 10% of their maximal activity (fig. S4f). In keeping with this empirical result, across successful model fits, the bias current to VIP cells was more positive than the bias current to SST cells (fig. 2c, fig. S7a). In the model, this differential bias current supported the VIP-dominated regime at small size and low contrast.

Next, we aimed to understand what shifts the network to an SST-dominated regime in response to large and high contrast gratings. With increasing size and contrast, we hypothesized that growing levels of PC activity could allow SST cells to overcome VIP cells' initial advantage in spontaneous input current and ultimately outcompete them (fig. 2d). This would be possible if SST cells could more effectively convert increases in PC activity to inhibitory SST→VIP current, than VIP could convert PC activity to inhibitory VIP→SST current. One possible mechanism would be if SST→VIP weights were larger than VIP→SST weights. Indeed, across successful model fits, SST→VIP weights were on average 110% stronger than VIP→SST weights (fig. S7b). Thus, in the model, powerful SST→VIP inhibition supported the SST-dominated regime at large size and high contrast.

We next asked how the network transitioned from the VIP-dominated to the SST-dominated regime. First, we expected that with increasing contrast, monosynaptic excitation from PCs should more strongly drive SST cells, and more weakly drive VIP cells. To test this hypothesis in the model, we computed "effective monosynaptic connection strengths" for each pair of cell types and for each stimulus condition. We defined effective monosynaptic connection strengths from the presynaptic population I to the postsynaptic population j as the synaptic weight matrix elements $w_{i\rightarrow j}$ multiplied by the slope of the postsynaptic firing rate nonlinearity φ_j. We examined effective connection strength at 22°, a size at which we observed surround suppression at the highest contrast and nearly flat size tuning at low contrast. Consistent with the conceptual explanations presented above, we found that during spontaneous activity, PC→VIP effective connection strength outweighed that of PC→SST (fig. 2e). PC→VIP effective connection strength then gradually decreased with increasing contrast,

307 while PC→SST effective connection strength gradually increased (fig. 2e), ultimately overtaking
308 it at 50-100% contrast. This suggested that as contrast increases, PCs more effectively recruit
309 SST cells compared with VIP cells, helping to explain the contrast-dependent shift from a VIP- to
310 an SST-dominated regime.
311 Having characterized the effective monosynaptic connection strength from PCs to SST
312 cells and VIP cells, we then asked how the full polysynaptic effect of PCs on these cell types, or
313 functional connectivity, changed with increasing contrast to shape their tuning. We simulated
314 the impact of small excitatory current injections to L2/3 PCs, propagating through the full
315 recurrently connected network, on VIP and SST firing rates (fig. 2f—see Methods). Indeed, as
316 contrast increased, driving PC activity increasingly drove SST cells, but increasingly suppressed
317 VIP cells. In fact, by simulating current injections of increasing, finite magnitude to PCs starting
318 from spontaneous activity, we were able to reconstitute opposing tuning of SST and VIP cells,
319 with SST cells showing superlinear responses to increasing PC activity, and VIP cells showing
320 bandpass responses, peaking at intermediate levels of PC activity (fig. S7c). Deleting either the
321 VIP bias current (fig. S7d) or the SST→VIP weight from the model (fig. S7e) abolished this
322 behavior, tipping the competition in favor of SST and VIP cells, respectively, across contrasts.
323 This supported the idea that a large stimulus-independent current to VIP cells competes with
324 strong stimulus-dependent SST→VIP inhibition to support opposing regimes of VIP and SST
325 activity depending on stimulus size and contrast.
326 To understand the significance of these opposing regimes of VIP and SST activity, we
327 then examined the monosynaptic connectivity of the VIP-SST subnetwork across cortical space.
328 Above, we proposed that SST activity should support surround suppression by participating in
329 disynaptic inhibition across space. If this were true, we would expect that SST cells should
330 strongly integrate inputs across the two modeled spatial domains. Indeed, across successful
331 model fits, SST cells had substantially higher cross-space weight than the other three L2/3 cell
332 types (fig. 2g). Next, we expected that PC-SST feedback could be important for promoting
333 competition between PCs across space. In turn, we reasoned that PC-VIP feedback might
334 suppress competition by controlling tuning of SST cells (fig. 2h).
335 To measure cooperation and competition between PCs across cortical space in the
336 model, we simulated the effect of excitatory current injections to L2/3 PCs in the surround, on
337 L2/3 PCs in the center. The model predicted surround PCs should increasingly suppress center
338 PCs with increasing contrast (fig. 2i). To test the importance of PC-SST feedback for this
339 contrast-dependent competition, we deleted PC→SST connections, allowed the rest of the
340 network to settle to a new steady state, and then repeated the activation of surround L2/3 PCs
341 as before. Eliminating this connection promoted cooperation at all contrasts, and weakened the
342 contrast dependence of this competition overall (fig. 2i,j), demonstrating that in the model, PC-
343 SST negative feedback is critical for contrast-dependent competition across space. Deleting
344 PC→VIP connections in a similar way promoted competition across all contrasts, and weakened
345 the contrast dependence of this competition overall (fig. 2i,j). This demonstrated that in the
346 model, a balance of negative PC-SST feedback and positive PC-VIP feedback is necessary for the
347 contrast dependence of cooperation and competition between PCs across space.
348
349 **Optogenetic dissection of the VIP-SST subnetwork's role in contrast dependent surround**
350 **suppression**

The computational model explained that PC-SST feedback supports competition between PCs across space, while PC-VIP feedback supports cooperation. This implies that VIP cells might directly shape the tuning of SST cells. Indeed, the model predicted that suppressing VIP cells would significantly alter the response properties of SST cells (fig. 3a). To empirically test this, we examined the impact of optogenetically silencing VIP cells on SST responses using simultaneous one photon optogenetics and two photon calcium imaging. We simultaneously measured neural activity in VIP cells, SST cells, and PCs (see Methods and fig. S8) while silencing VIP cells using Cre-dependent eNpHR3.0. We first confirmed the efficacy of optogenetic silencing of VIP cells (fig. S9b). Red illumination through the microscope objective robustly suppressed activity in eNpHR3.0-expressing VIP cells approximately linearly across stimuli by about 67% (fig. S9c-h, $R=0.91$, $p=1x10^{-9}$).

Consistent with model predictions, silencing VIP cells potently facilitated SST cells across all sizes and contrasts (fig. 3b). This demonstrated that VIP cells crucially regulate visually driven SST-activity. More importantly, we next asked whether the remarkable insensitivity of SST cells to low contrast stimuli could be explained by inhibition from VIP cells. If VIP activity is necessary for tuning the contrast sensitivity of SST cells, silencing VIP cells should preferentially facilitate SST responses to low contrast. Indeed, we found that silencing VIP cells preferentially potentiated SST cells' responses to low contrast (fig. 3c), and only more weakly facilitated SST responses to high contrast (fig. 3d). This was true across sizes (fig. 3e,f). As a result, the sensitivity of SST cells to contrast increased significantly, measured as a decrease in the C_{50} of their contrast tuning across sizes (fig. 3g, $p < 0.05$, Wilcoxon signed-rank test). This demonstrates that VIP cells shape the contrast sensitivity of SST cells by strongly suppressing their responses to low contrast.

Having established that VIP activity was necessary for suppressing SST responses to low contrast, we next asked how this effect would propagate through the network polysynaptically to PCs, which only receive weak or sparse monosynaptic inhibition from VIP cells (Pfeffer et al., 2013). Because intrinsic firing rate nonlinearities in L2/3 PCs have been found to give rise to non-intuitive asymmetries in optogenetic perturbations (Phillips & Hasenstaub 2016), we measured the impact on PCs of both activation and silencing of VIP cells. A previous model of this microcircuit predicted that disconnecting VIP cells from the network (equivalent to completely silencing them) would suppress PC responses selectively to low contrast, while leaving responses to high contrast unaffected (Millman et al., 2019). However, because superlinearity was a key driver of tuning properties in our network model, one might predict the opposite: that silencing of VIP cells could more strongly suppress PCs at high contrast, when PCs are at a more sensitive point in their firing rate nonlinearity (see schematic, fig. 4a). We conceived a purely phenomenological simple superlinear model, in which the effect of bidirectional (silencing or activating) optogenetic perturbations on response to a given stimulus linearly increases with increasing network activity in the control (light off) condition (fig. 4b). By contrast, in a simple linear model, the effect of optogenetic perturbations would be constant with respect to control activity level. This phenomenological model allowed us to partition optogenetic effects into two components: a component that could be explained purely by the activity level in control conditions for a specific visual stimulus (fig. 4c), and a residual component that could not (fig. 4d). We reasoned that this residual component, not explained

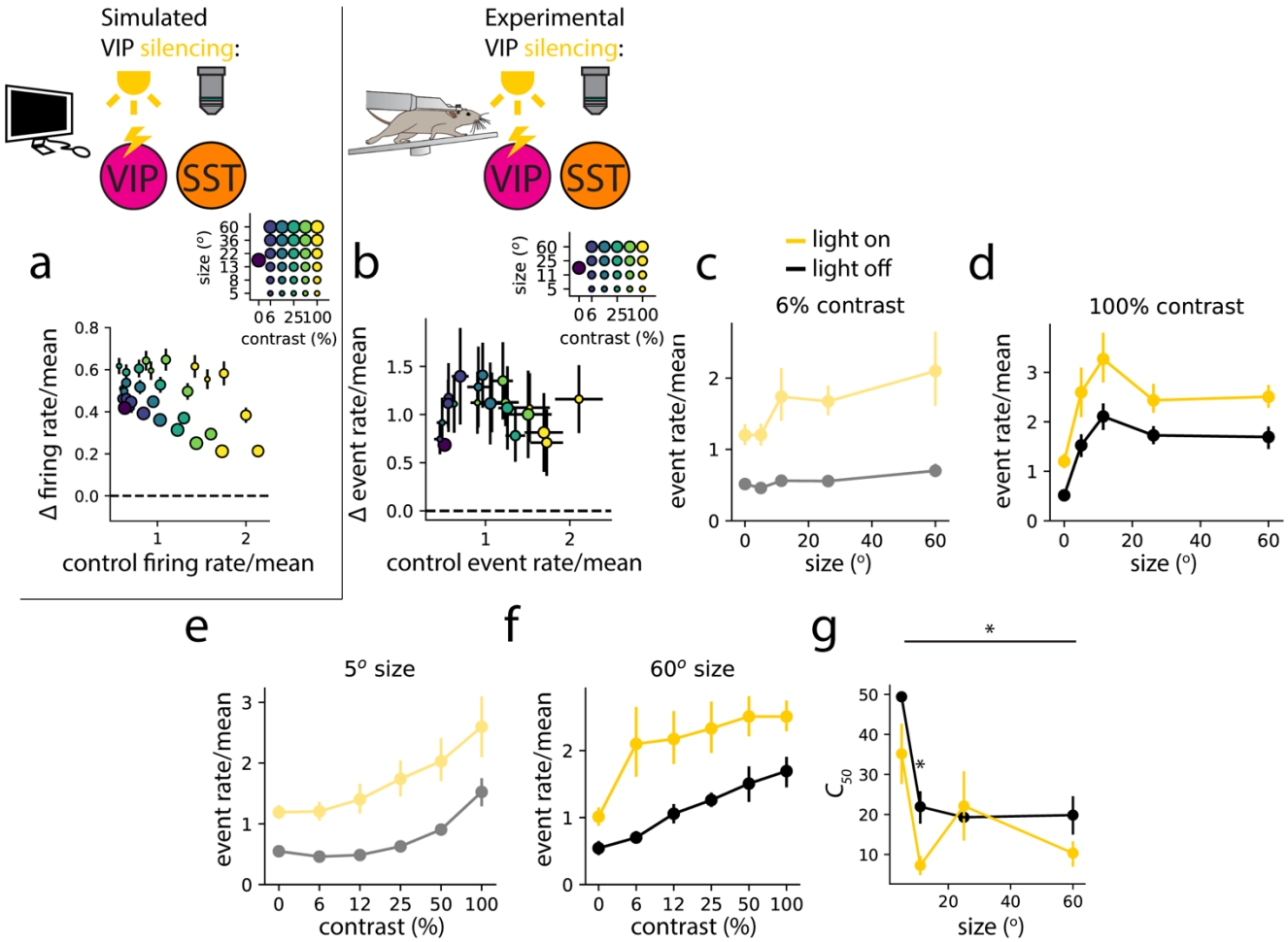

Figure 3. VIP suppression enhances responses of SST cells to low contrast. A) Model: predictions for the impact of inhibitory current injection to VIP on the responses of SST cells to gratings of various contrasts and sizes. Shown is a scatter plot of SST event rate with light off, vs. difference between light on and light off, for stimuli of varying size (dot size) and contrast (dot color—increasing from cold to warm colors). B) Same as A), but for experimental VIP silencing. C) SST event rate as a function of size, at 6% contrast, in the light off (black) and light on (yellow) condition. D) Same as C), for 100% contrast. E) SST event rate as a function of contrast, at 5° size. F) Same as E), for 60° size. G) C_{50} as a function of size. C_{50} is significantly reduced by VIP silencing at the 11° size, and across sizes. Error bars represent bootstrap SEM equivalent.

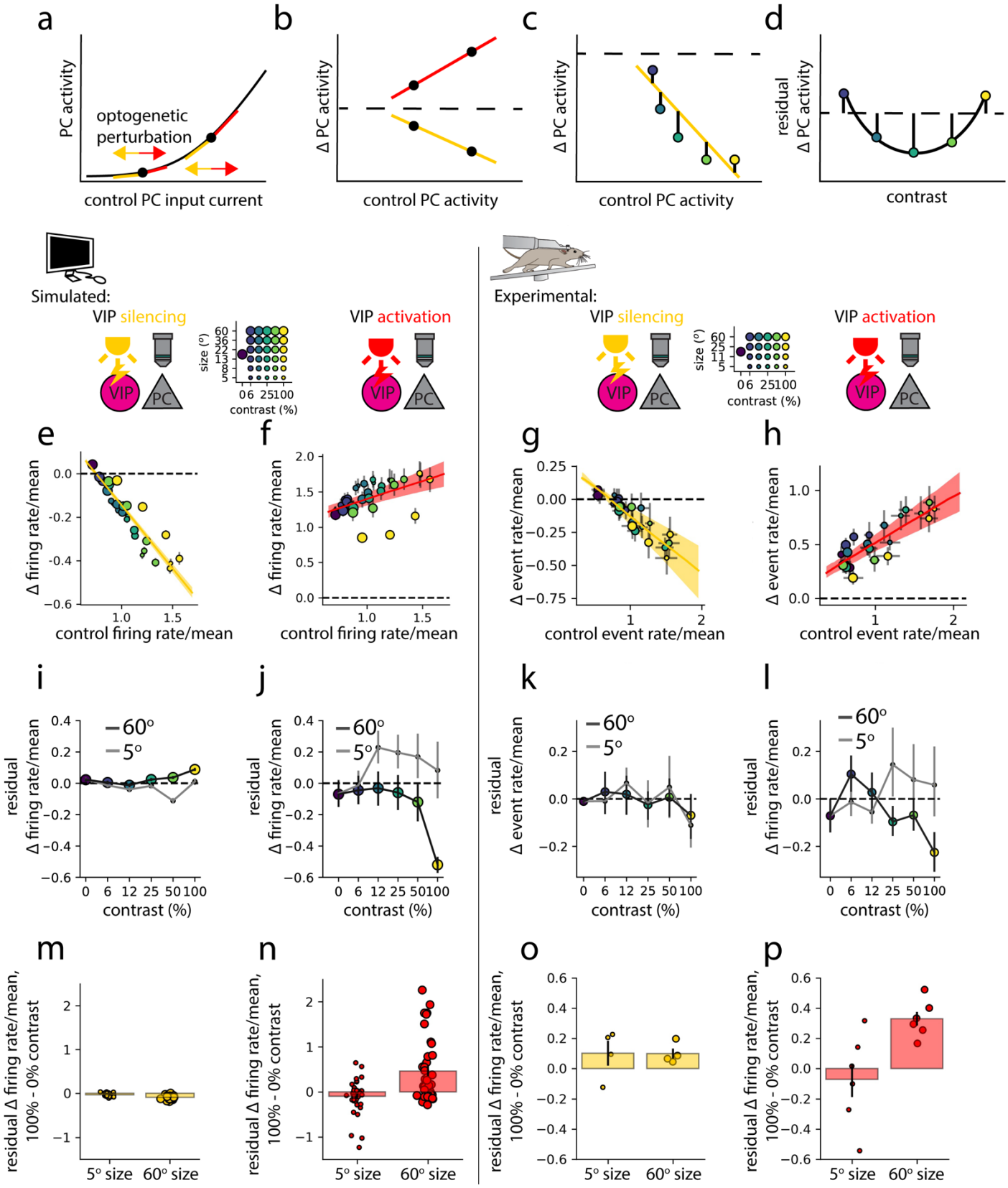
a
PC activity
optogenetic perturbation
control PC input current
b
Δ PC activity
control PC activity
c
Δ PC activity
control PC activity
d
residual Δ PC activity
contrast
Simulated:
VIP silencing
VIP activation
size (°)
contrast (%)
Experimental:
VIP silencing
VIP activation
e
Δ firing rate/mean
control firing rate/mean
f
Δ firing rate/mean
control firing rate/mean
g
Δ event rate/mean
control event rate/mean
h
Δ event rate/mean
control event rate/mean
i
residual Δ firing rate/mean
60°
5°
contrast (%)
j
residual Δ firing rate/mean
60°
5°
contrast (%)
k
residual Δ event rate/mean
60°
5°
contrast (%)
l
residual Δ firing rate/mean
60°
5°
contrast (%)
m
residual Δ firing rate/mean, 100% - 0% contrast
5° size
60° size
n
residual Δ firing rate/mean, 100% - 0% contrast
5° size
60° size
o
residual Δ firing rate/mean, 100% - 0% contrast
5° size
60° size
p
residual Δ firing rate/mean, 100% - 0% contrast
5° size
60° size

Figure 4. Network superlinearity explains experimental and simulated effects of bidirectional VIP manipulations, in simulation and experiment. A) Schematic model for predicting the effects of VIP perturbations. PC activity is intrinsically superlinear, with both network suppression and network facilitation increasing in strength with increasing network activity. B) If the effect of optogenetic perturbation is entirely described by a superlinear curve, as in A), the light on – light off activity (Δ activity) given light off (control) activity will fall along a monotonically increasing (decreasing) curve for facilitating (suppressing) perturbations. If the curve in A) is an exponential, the curve describing changes in activity is a straight line. C) Schematic scatter plot of Δ activity, vs. control activity, with best fit line in yellow. "Residual" effects are defined as the difference between the actual change in activity, and best fit line. D) Schematic plot of residual effects vs. contrast. E) Scatter plot of PC Δ firing rate vs. control firing rate for simulated inhibitory current injection to VIP, with L4 activity held constant. In yellow is the least squares linear fit, with shading indicating bootstrap 68% confidence intervals. Dot size and color are as in fig. 3A. F) Same as A), for simulated excitatory current injection to VIP. In red is the least squares linear fit, with shading indicating bootstrapped 68% confidence intervals. G) Experimentally measured Δ PC event rate in response to VIP silencing, vs. control event rate. Linear fit is plotted as in C). H) Same as G), but for VIP activation.. I) Residual effect of simulated VIP inhibitory current injection in E) not captured by the best fit line. J) Same as I), but for simulated VIP excitatory current injection in F. K,L) Same as I), J), but for experimental VIP silencing and activation, respectively, in G),H). M-P) Residual effect at 100% - 0% contrast, for 5° and 60° size, for data in I-L), respectively. Error bars indicate bootstrap SEM equivalent. Shading on fit lines indicates 68 percent confidence interval of linear fits.

395 simply by network superlinearity, might be informative of recurrent network mechanisms.
396 Using our network model, we could then separately probe the roles of modeled synaptic
397 connections in generating each component.
398 First, we sought to distinguish whether our network model was operating in the regime
399 exemplified in (Millman et al., 2019), or in a regime where superlinearity dominated responses
400 to optogenetic perturbations. If the latter were true, the simple superlinear model should
401 capture much of the optogenetic effects. Because our network model took L4 PC activity as
402 feedforward input, it was first necessary to measure the direct effects of bidirectional VIP
403 manipulations on L4 PCs (see fig. S10a,b and Methods). We then simulated bidirectional current
404 injections to VIP cells, combined with the empirically measured bidirectional effects on L4 PCs.
405 Across a range of simulated current injection magnitudes, the full recurrent network model
406 predictions were broadly in line with the simple superlinear model, with higher control firing
407 rates predicting stronger suppressive effects of VIP silencing (fig. 4e, R=-0.72, p=0.0, Wald test)
408 and stronger facilitating effects of VIP activation (fig. 4f, R=0.16, $p=2x10^{-13}$, Wald test). This
409 agreed with the simple superlinear model prediction, and contrasted with the prediction of
410 (Millman et al., 2019). This was true also when excluding the effect of VIP manipulations on L4
411 PCs in the model (fig. S11). Our network model predicted that despite VIP cells' low activity
412 level at high contrast, perturbations to VIP cells would be differentially amplified by the
413 network depending on the strength of PC activity in control conditions, thus increasing with
414 contrast overall.
415 To test this model prediction experimentally, we virally expressed Cre-dependent
416 eNphR3.0-mRuby3 or ChrimsonR-tdTomato in VIP cells in separate mice, and gCaMP6s in all
417 L2/3 neurons using the hSynapsin promoter (see Methods). As with VIP silencing, we confirmed
418 the efficacy of optogenetic activation of VIP cells. Red illumination through the microscope
419 objective drove robust activity in ChrimsonR-expressing VIP cells across stimulus conditions (fig.
420 S12a,b), although optogenetic facilitation was somewhat stronger for small and low contrast
421 stimuli (fig. S12c-h). Importantly, in control mice expressing no opsin, the optogenetic
422 stimulation light alone produced no systematic facilitation or suppression of visual responses
423 (fig. S13). This confirmed that the observed effects were due to the optogenetic perturbation
424 *per se*. Next, we analyzed the impact of perturbing VIP cells on the activity of all gCaMP6s-
425 expressing neurons not labeled with a red fluorophore (primarily PCs). In both VIP silencing and
426 VIP activation experiments, PC responses with the optogenetic light off agreed well with
427 responses we measured previously using calcium imaging in transgenic gCaMP-expressing mice
428 (fig. S14; VIP silencing, R=0.95, $p=3x10^{-12}$, Wald test; VIP activation, R=0.84, $p=3x10^{-7}$, Wald
429 test). As predicted by the full recurrent network model, across stimulus conditions, high PC
430 activity in control conditions predicted stronger suppressing effects of VIP silencing (fig. 4g, R=-
431 0.64, $p=2x10^{-12}$, Wald test), and stronger facilitating effects of VIP activation (fig. 4h, R=0.45,
432 $p=2x10^{-8}$, Wald test).
433 Importantly, the simple superlinear model, in which control activity levels completely
434 determined the effect of optogenetic perturbations, could explain much but not all of the effect
435 of bidirectional VIP manipulations on PC activity. We next examined the residual effects of
436 optogenetic perturbations that were not captured by the simple superlinear model: specifically,
437 the difference between the actual change in activity and the best fit line prediction of change in
438 activity from control activity. We reasoned that these residuals might shed light on the

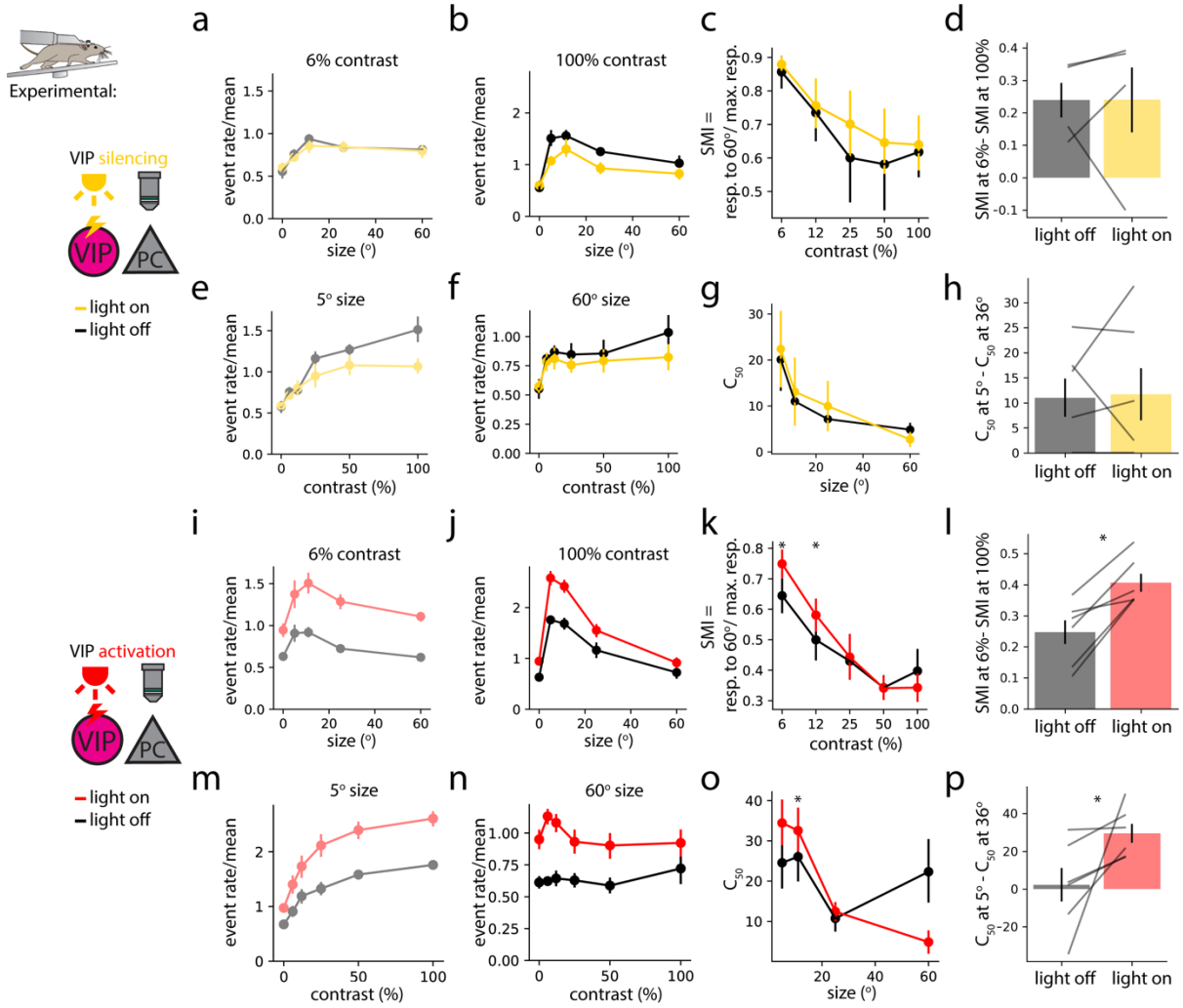

Figure 5. VIP activation unidirectionally enhances contrast-dependent surround suppression. A) Size is plotted on the x-axis, and PC event rate on the y-axis, for 6% contrast, the lowest tested, in the light off condition (black) and light on condition (yellow). B) Same as A) for 100% contrast. C) Surround modulation index is plotted as a function of contrast, in the light on and light off conditions. D) Change in SMI between the light off and light on condition, with each line an experiment. E) Same as A), B), but responses to increasing contrast are plotted for fixed 5° size, in the light off and light on condition. F) Same as E), but for 60° size. G) C_{50} is plotted as a function of size, for the light off and light on conditions. H) Bar plot of change in C_{50} between 5° and 60° size, for the light off and light on conditions, with lines indicating individual imaging sessions. I-P) Same as A-H), but for optogenetic activation of VIP cells. * significant difference, $p < 0.05$ (Wilcoxon signed-rank test). Error bars indicate bootstrap SEM equivalent.

recurrent network mechanisms that mediate the contrast dependent shift from cooperation to competition via the VIP-SST network. If competition between PCs across space increased with increasing contrast, as predicted by the recurrent network model, we might expect this to support a strong negative feedback loop at high contrast, limiting the network's response to VIP activation at high contrast but permitting it at low contrast. We optimized the magnitude of excitatory and inhibitory current injected to VIP cells for each model fit, to maximize dynamic range of PC competition across space (see Methods and fig. S17). Although modeled residual effects of VIP silencing were small (fig. 4i), modeled residual effects of VIP activation were in keeping with this prediction (fig. 4j). PC facilitation in response to VIP activation was stronger than expected by the simple superlinear model at low contrast, and weaker than expected at large size and high contrast. Experimental results of VIP silencing (fig. 4k) and activation (fig. 4l) showed a similar asymmetry. Across all conditions, VIP activation at 60° size showed the strongest contrast dependence of residuals, defined as the residual effect at 100% contrast – 0% contrast (fig. 4m-p).

We then asked how this asymmetric contrast-dependent residual effect of bidirectional VIP manipulation affected contrast-dependent surround suppression in the experimental data. Although VIP silencing significantly suppressed visual responses across most stimuli (Fig. 5a,b), it did not significantly affect the surround modulation index (SMI) at any contrast (fig. 5c), and thus there was no significant change in ΔSMI between 6% and 100% contrast (fig. 5d). Similarly, there was no significant change in contrast sensitivity at any size (fig. 5e-h). We corroborated these calcium imaging results by recording neural activity using extracellular electrophysiology in a separate cohort of mice. In these electrophysiological experiments, we also compared the optogenetic effects between the non-locomoting an the locomoting condition (fig. S15), and as above, saw no brain-state dependent difference. We also found similar effects in RS and FS units (fig. S15). These measurements confirmed that VIP silencing did not substantially alter the contrast dependence of surround suppression.

On the other hand, VIP activation enhanced visual responses across all conditions. For the same control activity level, activating VIP cells disproportionally facilitated PCs in response to large, low contrast stimuli (fig. 5i), but less so for large, high contrast stimuli (fig. 5j). As a consequence, VIP activation enhanced the contrast dependence of surround suppression overall, evident as an increase in SMI specifically at low contrast (fig. 5k,l) and an increase in ΔSMI between 6% and 100% contrast. This change in contrast-dependent surround suppression could not be explained by the simple superlinear model alone (fig. S16), and therefore was a result of the asymmetric contrast-dependent residual effects of VIP activation. Similarly, VIP activation increased size dependence of contrast sensitivity (fig. 5m-p).

We next returned to our recurrent network model to ask whether this asymmetric contrast-dependent residual effect of VIP activation was tied directly to contrast dependent spatial competition between PCs. If this were the case, we would expect manipulations that suppressed the contrast dependence of PC spatial competition to suppress the contrast dependence of residual effects of VIP activation. Previously, we found that the contrast dependence of PC spatial competition in the model depended on an interplay between two feedback loops: a PC-VIP feedback loop, primarily active at low contrast, and promoting cooperation, and a PC-SST feedback loop, primarily active at high contrast, and promoting competition. Having established that these feedback loops supported the contrast dependence

483 of PC spatial competition, we next asked whether they also supported the contrast-dependent
484 residual effect of VIP activation on PC responses that was evident in our previous simulations.
485 While deleting PC→VIP weights or PC→SST weights only weakly affected simulated responses
486 to VIP silencing (fig. 6a,b respectively), the same manipulation dramatically reduced simulated
487 responses to VIP activation (fig. 6c,d respectively). Similarly, these manipulations significantly
488 and asymmetrically reduced residual effects of VIP activation, and not silencing (fig. 6d-g), as
489 well as the contrast dependence of these residuals (fig. 6h-k). This suggested that the
490 asymmetric contrast-dependent residual effect of VIP activation, which was necessary for
491 enhancement of contrast-dependent surround suppression, was a result of contrast-dependent
492 spatial cooperation and competition between PCs. The model predicted that this asymmetric
493 residual effect at low contrast was a generic result of facilitating feedforward drive to the L2/3
494 network, not only via manipulation of VIP activity (fig. S10c,d). Further, the asymmetry could be
495 explained by enhanced contrast dependence of positive PC-VIP feedback specific to moderate
496 increases in PC and VIP activity, with decreases in activity, and large increases in activity,
497 causing a much weaker reduction in this contrast dependence (fig. S17). Thus, modeling results
498 supported the idea that residual effects of VIP activation we observed were signatures of
499 contrast-dependent competition between PCs across space, mediated by the VIP-SST
500 subnetwork.
501
502 **Recurrent amplification drives the network superlinearity that enforces contrast dependent**
503 **surround suppression**
504
505 Our modeling and optogenetic results suggested that network superlinearity critically shapes
506 cooperative and competitive interactions across space, and thus the sensory code. To address
507 the origin of this superlinearity, we considered two possibilities: it could be generated purely by
508 the cell-intrinsic firing rate nonlinearity, or also steepened by PC-PC recurrent excitation. To
509 distinguish between these two possibilities, we simulated the effect of direct current injection
510 to PCs in several conditions. First, to isolate the cell-intrinsic response, we deleted all synaptic
511 connections in the network and compared this to the intact condition. Deleting all connections
512 made network nonlinearity much more shallow (fig. 7a, black solid black versus dashed black
513 line). This suggested that recurrent circuits contributed substantially to network superlinearity.
514 Next, we selectively deleted PC-PC weights while leaving all other connections intact. This
515 yielded a substantially shallower response to current injection than the full network response,
516 and shallower even than the cell-intrinsic firing rate nonlinearity alone (Fig. 7a, gray solid line).
517 This suggested that PC-PC recurrent excitation is critical to this superlinearity, and in its
518 absence, powerful feedback inhibition from PV cells may suppress network superlinearity even
519 below the cell-intrinsic nonlinearity. To test this, we deleted all recurrent connections among
520 the PC-PV subnetwork (PC-PC, PC-PV, and PV-PV), while leaving all other connections intact. In
521 this scenario, current injections to PCs yielded a superlinear response similar to the cell-intrinsic
522 firing rate nonlinearity alone (Fig. 7a, blue line). Notably, deleting PC-PV connections alone
523 drove the network to instability (data not shown). Thus, within the network model, recurrent
524 amplification by the PC-PV subnetwork generated a second and more powerful network
525 nonlinearity, building on the cell-intrinsic firing rate nonlinearity.

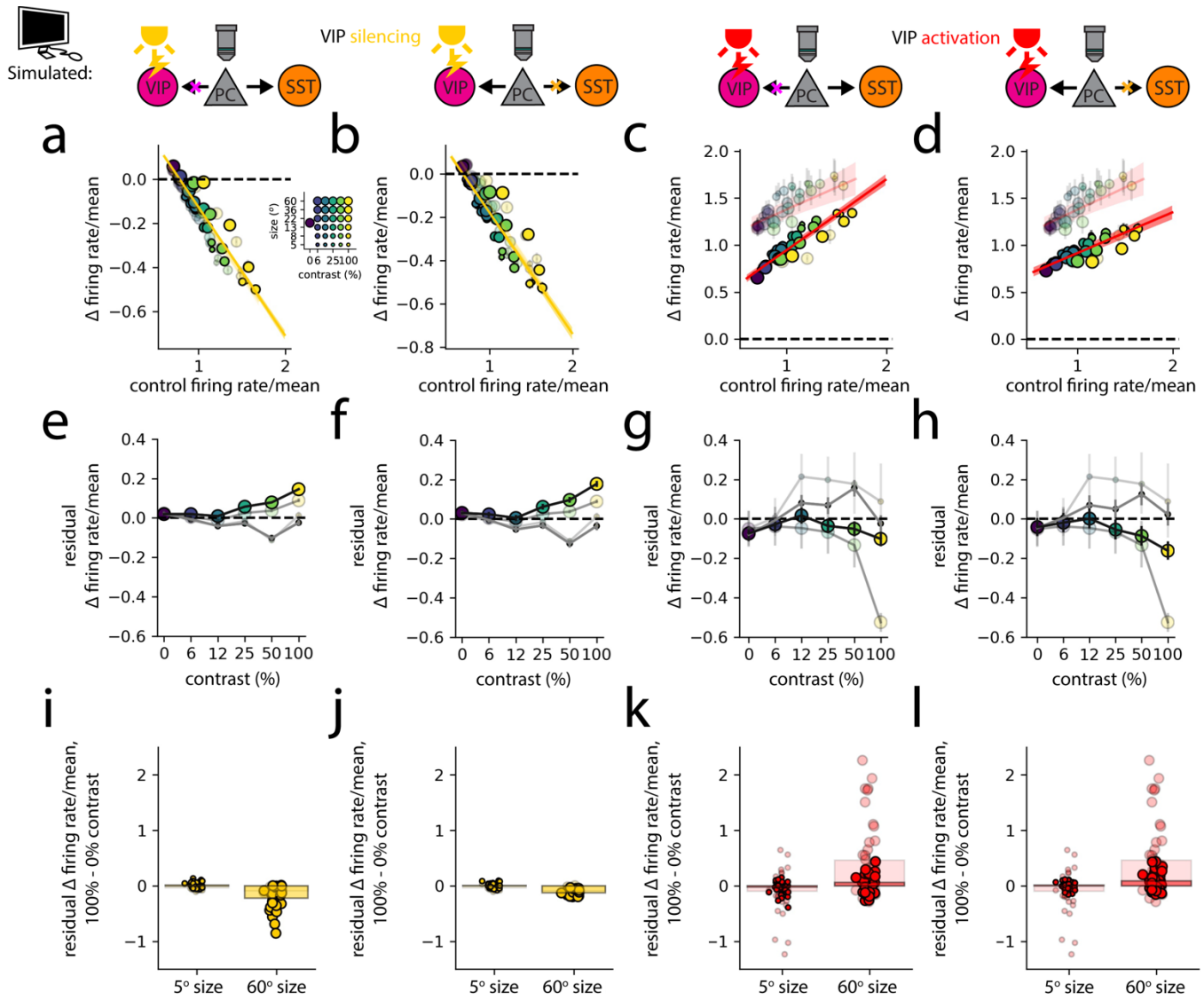

Figure 6. Asymmetric residual effect of VIP perturbation reflects contrast-dependence of PC-VIP and PC-SST feedback loops in simulation. A) Scatter plot of modeled change in firing rate, vs. control firing rate, both normalized to mean across stimuli, in response to inhibitory current injection to VIP cells, after deleting PC→VIP connections. Transparent dots and lines in all panels correspond to the baseline condition, without deleting any connections. Dot size and color are as in fig. 3A. B) Same as A), after deleting PC→SST connections, respectively. C,D) Same as A), B), but for modeled excitatory current injection to VIP cells. E-H) Residual effect of VIP silencing and activation in A-D), respectively, defined as effect minus expectation based on linear fit to control (light off) firing rate. I-L) Residual effect at 100% - 0% contrast, for 5° and 60° size, for data in E-H), respectively. Error bars indicate bootstrap SEM equivalent. Shading on fit lines indicates 68 percent confidence interval of linear fits.

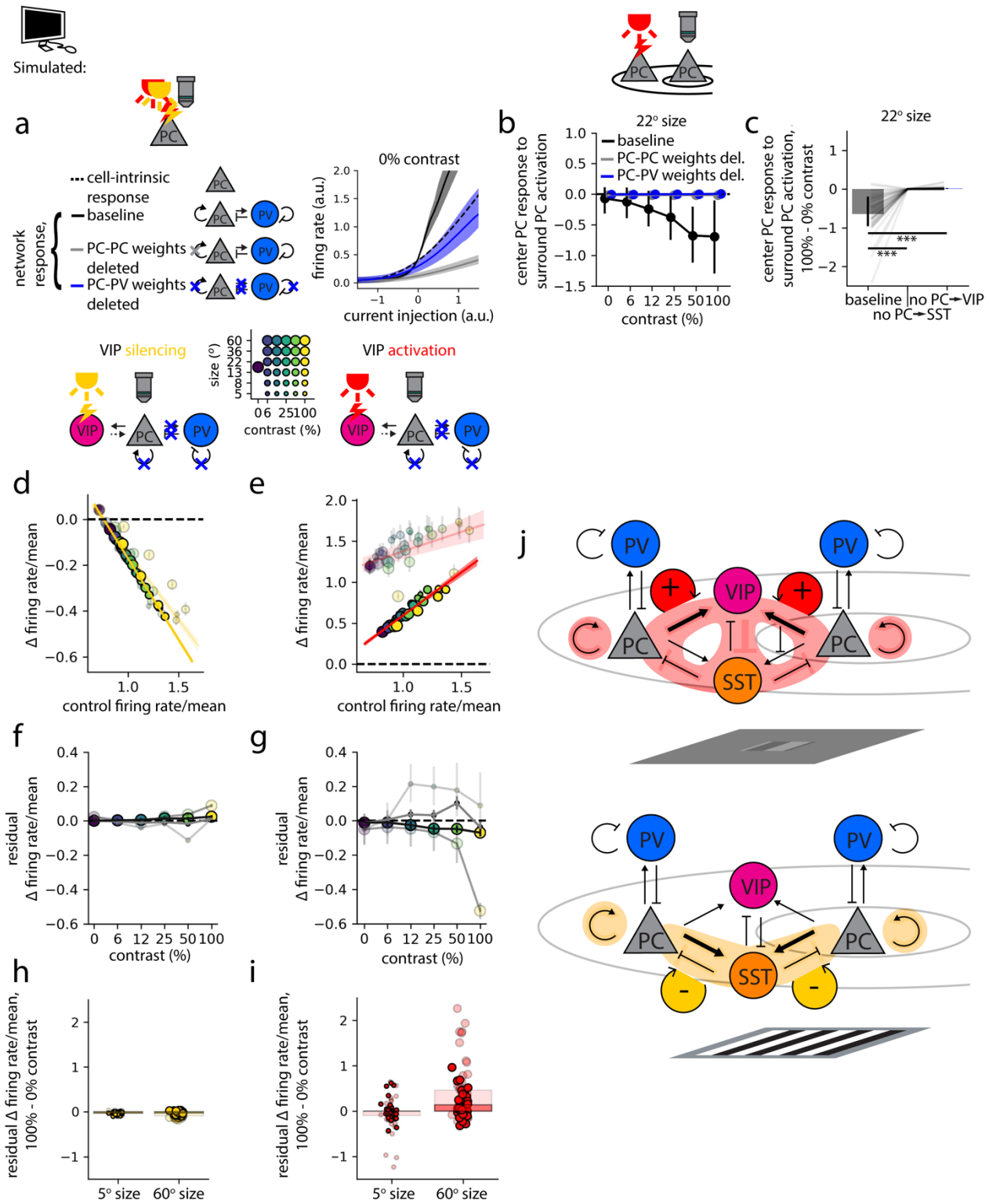

Figure 7. A positive PC-PV feedback loop enhances contrast-dependent surround suppression in simulation. A) Schematic of modeled perturbations. We measure the response of simulated neurons for (1) no network connections (cell-intrinsic response), (2) the baseline

condition (all connections intact), (3) PC-PC connections selectively deleted, and (4) PC-PC, PC-PV, and PV-PV connections deleted. Plotted at right is the simulated L2/3 PC firing rate in response to direct current injections to L2/3 PCs, vs. the current injected, for the four conditions considered, at the 0% contrast condition. Shading indicates 16th to 84th percentile. B) Simulated response of L2/3 center PCs to excitatory current injection to L2/3 surround PCs, for 22° size, at increasing contrast. Also plotted are the same responses for PC-PC connections deleted, or all recurrent connections among PCs and PV cells deleted. C) The difference between center PC responses to surround PC activation at 100% contrast, and 0% contrast, at 22° size, for the baseline case, and after deleting PC-PV connections, or all connections among PCs and PV cells. At baseline, the difference is significantly larger across successful model fits ($p < 10^{-7}$, $p < 10^{-7}$, Wilcoxon signed-rank test). D) Scatter plot of simulated change in L2/3 PC activity vs. baseline activity in response to inhibitory current injection to VIP cells, plus empirically measured suppression of L4 PCs, after deleting all recurrent connections among PCs and PV cells. Transparent dots and lines in all panels correspond to the baseline condition, without deleting any connections. Dot size and color are as in fig. 3A. E) Same as D), but for simulated excitatory current injection to VIP cells, plus empirically measured facilitation of L4 PCs (same as 4F), after deleting all recurrent connections among PCs and PV cells. F,G) Residual effect of VIP perturbation in D), E), respectively, defined as effect minus expectation based on linear fit to baseline firing rate. H, I) Residual effect at 100% - 0% contrast, for 5° and 60° size, for data in F), G), respectively. J) Schematic summarizing primary findings. At low contrast and small size, VIP cells are highly active, enhancing the effective weight of the PC-VIP connection. This results in a disinhibitory positive feedback loop, facilitating PC responses and promoting cooperation among PCs. At high contrast and large size, SST cells are highly active, enhancing the effective weight of the PC-SST connection. This results in a negative feedback loop, suppressing PC responses and promoting competition among PCs. Recurrent amplification within the PC-PV subnetwork strengthens both the positive PC-VIP and negative PC-SST feedback loops. Error bars in B), C) indicate 16th to 84th percentile of model fits. Error bars in D-G) indicate bootstrap SEM equivalent. Shading on fit lines indicates 68 percent confidence interval of linear fits.

We next asked what role intrinsic connections within the PC-PV subnetwork played in shaping contrast-dependent cooperation and competition of PCs across space. Consistent with recurrent PC-PV connections amplifying the effect of contrast-dependent PC-VIP and PC-SST feedback loops, we found that in the absence of connections among PCs, or among PCs and PV cells, PC competition across space depended much more shallowly on contrast (fig. 7b,c). Because superlinearity could explain the control activity dependence of VIP optogenetic effects, we reasoned that the PC-PV network could powerfully shape this dependence, via the steepness of the network nonlinearity. We next asked how the network nonlinearity generated by recurrent PC-PV connections shaped the impacts of VIP perturbations on PCs. To this end, we simulated optogenetic VIP activation as before with the full network intact, or when deleting recurrent weights among PCs and PV cells. Based on the enhancement of network superlinearity by recurrent weights among PCs and PV cells, we first expected that the activity dependence of PC responses to VIP perturbations (as captured by the simple superlinear model above) would be strongly affected. Indeed, while effects of simulated VIP silencing were only modestly affected by deleting weights in the PC-PV subnetwork (fig. 7d), across stimuli, the same manipulation substantially reduced the effects of simulated VIP activation (fig. 7e).

Previously, we found that this contrast-dependent spatial competition had signatures in the residual effects of bidirectional VIP perturbations, compared to the predictions of a purely superlinear prediction. In principle, we reasoned that positive feedback loops within this subnetwork could shape the residual effects we observed above, by amplifying the strength of the PC-VIP and PC-SST feedback loops shaping PC competition across cortical space. Based on our simulations of deleting PC-VIP and PC-SST connections, we predicted that the reduced contrast dependence of spatial competition we observed after deleting connections in the PC-PV subnetwork would result in a dramatic reduction in residual effects of VIP activation on PC responses at low contrast. As shown above, for the intact network, VIP silencing generated small residual effects on PCs; deleting recurrent PC-PV weights dampened even these small residual effects. For the intact network, VIP activation generated a large contrast-dependent residual effect on PCs (fig. 7i) and deleting recurrent PC-PV weights severely dampened these residual effects (fig. 7j). This suggested that, within our simulations, the small and low contrast-selective effect of VIP activation, depends critically on positive feedback loops within the PC-PV subnetwork. Thus, the model explains that PC-PV recurrent amplification sets up a steep network superlinearity that synergizes with a PC-VIP positive feedback loop at small size and low contrast to favor cooperation across space, and with a PC-SST negative feedback loop at large size and high contrast to favor competition (fig. 7k).

Discussion

We combined experiments and computational modeling to address the circuit mechanisms that gate cooperation and competition across cortical space. We studied contrast-dependent surround suppression in the primary visual cortex as a paradigmatic example of such flexible cooperation and competition. Although discovered more than two decades ago, a circuit mechanism for how the same cortical circuit dynamically shifts between a cooperative and competitive operating regime based on the size and contrast of the visual stimulus has been lacking. As the same cell types and circuits exist throughout cortical areas, the findings of this

570 study may generalize beyond the visual cortex to more broadly explain how cortical circuits
571 adjust functional interactions across cortical space to meet task demands.
572 Through a combination of calcium imaging, electrophysiology, optogenetic
573 perturbations, and network modeling, we show that a transition from positive PC-VIP feedback
574 at low contrast, to negative PC-SST feedback at high contrast, explains the contrast dependence
575 of surround suppression. Because SST cells strongly integrate PC inputs across space, these
576 positive and negative feedback loops couple PCs across space. The PC-PV subnetwork amplifies
577 the strength of both feedback loops. We tested core predictions of this model experimentally
578 by optogenetically perturbing VIP cells. First, as predicted by the superlinearity of the network,
579 both VIP silencing and activation have the strongest effects when PC activity is highest, namely
580 at small size and high contrast. On top of this activity-dependent effect, VIP activation had a
581 large, asymmetric residual effect that was unexplained by PC activity level, positive at low
582 contrast and negative at high contrast. Our network model explains that this residual effect is a
583 consequence of contrast-dependent PC competition across space. Further, due to network
584 superlinearity, building on the cell-intrinsic superlinearity, the contrast dependent
585 enhancement of PC-VIP positive feedback by VIP activation is stronger than the contrast-
586 dependent suppression of PC-VIP positive feedback by VIP silencing, contributing to the
587 asymmetry. We found the partitioning of optogenetic effects into an activity-dependent
588 component and a residual component to be important to our interpretation of the optogenetic
589 results. The asymmetric effects of VIP activation and inactivation on pyramidal cell tuning are
590 reminiscent of a recent study examining activation and inactivation of PV and SST cells in A1
591 (Phillips & Hasenstaub, 2016). Bidirectional perturbations, generally, are likely to provide
592 rigorous tests of a predictive understanding of network dynamics.
593 The data and modeling presented above highlight that understanding strongly
594 recurrently connected networks (within and beyond the cortex), requires a combination of
595 causal perturbations and computational modeling. Without causal perturbations,
596 computational models may be underconstrained. In contrast to the theoretical predictions of a
597 recent study (Millman et al., 2019), we found that the effect of removing VIP activity from the
598 network was not selective for low contrast stimuli, despite the fact that VIP activity was highest
599 for those stimuli in control conditions. On the other hand, inferring recurrent network
600 mechanisms from causal perturbations is likely to be difficult when unsupported by a
601 computational model. The contrast dependence of PC coupling to the VIP and SST subnetworks,
602 which our perturbations revealed, challenges the simplest linear intuitions of how the network
603 might operate. Iteratively developing new intuitions instructed by recurrent network models,
604 such as feedback loops and stabilization, may be crucial for developing a predictive
605 understanding of neural function. Because one study cannot explore all possible causal
606 perturbations, constraining models based on the results of multiple studies will likely become
607 increasingly important. Incorporating the constraint that our modeled network occupy an
608 inhibitory stabilized regime, established by causal perturbations in previous studies, was crucial
609 to our understanding of the mechanism of network superlinearity.
610 In this study we considered PCs, PV cells, SST cells, and VIP cells as homogenous
611 populations, and restricted most of our analysis to population averages. However, it is already
612 well appreciated that each of the cell types breaks down into distinct sub-classes with unique
613 physiological properties, anatomy, and circuit connectivity. Future work may uncover

subpopulations of the interneurons we studied playing dissociable roles. For example, VIP cells are transcriptionally diverse, and molecular markers such as cholecystokinin and calretinin (He, et al. 2016), could define functional subclasses of VIP cells. Tuning diversity of VIP cells, like transcriptional diversity, has also been found to correlate with cortical depth (Dipoppa, et al. 2018). Diversity in tuning properties may align with diversity of functional roles in the cortical microcircuit. A recent study in the somatosensory barrel cortex found that a subpopulation of VIP cells co-expressing ChAT exert an inhibitory influence on PCs specifically in response to weak stimuli (Dudai, et al. 2020). A combination of intersectional genetic techniques and optogenetics, or two photon optogenetics, could yield further insight in the functional roles of distinct VIP populations in sensory coding. Furthermore, other 5-HT3aR+ interneurons not expressing VIP, particularly in layer 1, have been shown to have similar tuning for sensory signals as VIP cells (Abs et al., 2018; Mesik et al., 2015). Future work could clarify the extent to which these cell types act in concert with VIP cells or play disparate roles to control sensory coding. In addition to discrete variability between sub-classes of each cell type, continuous variability could be important, both in synaptic connections and in tuning properties. Future work could seek to model this variability, which might generate further hypotheses to be tested with more sophisticated optogenetic perturbations.

Translaminar inhibitory as well as excitatory connections are also likely to be important, particularly as VIP manipulations affect L4 as well as L2/3 activity. Future work expanding the scope of these experiments could clarify the extent to which translaminar feedforward and feedback connections shape the response properties of these cell types. Further, these cell types might differentially integrate feedback signals from higher areas (Keller, Roth, & Scanziani, 2020; Zhang et al., 2014), which could be important for their encoding of homogeneous textures as well as richer stimuli.

Furthermore, although we argue that the influence of VIP cells is likely to be important for network regimes optimizing detection, this study has examined only passively viewing mice, not animals motivated to detect weak signals. Behavioral context and salience of sensory inputs has been found to powerfully shape the tuning properties of these interneuron types, possibly to enhance coding properties of pyramidal cells. Future work combining two photon imaging of these cell types with behavior and network modeling could suggest possible dynamical mechanisms for this enhancement.

Despite these limitations, there is growing evidence that the circuit motifs examined in this study may generalize to other areas of the brain. In particular, in auditory cortex, a series of recent studies have uncovered analogous tuning properties and functional roles of the same interneuron types. VIP cells show bandpass tuning for sound amplitude (analogous to contrast) (Mesik, et al. 2015), while SST cells are insensitive to all but high amplitude tones (Li, Xiong, et al. 2015). Whereas PCs commonly prefer narrow spectral bandwidth (analogous to size) (Li et al. 2019), SST cells prefer broader spectral bandwidth (Lakunina et al., 2020). Silencing SST cells results in a reduction of lateral inhibition (Kato, Asinof and Isaacson 2017) and a facilitation of PC responses to broad spectral bandwidth sounds (Lakunina et al., 2020). Future work could examine the extent to which the L2/3 microcircuit in V1 and A1 occupies a similar dynamical regimes, and examine tuning properties of interneurons in S1 for space and intensity. How these insights extend to non-sensory cortices is an exciting area for future study.

Supplementary Figures

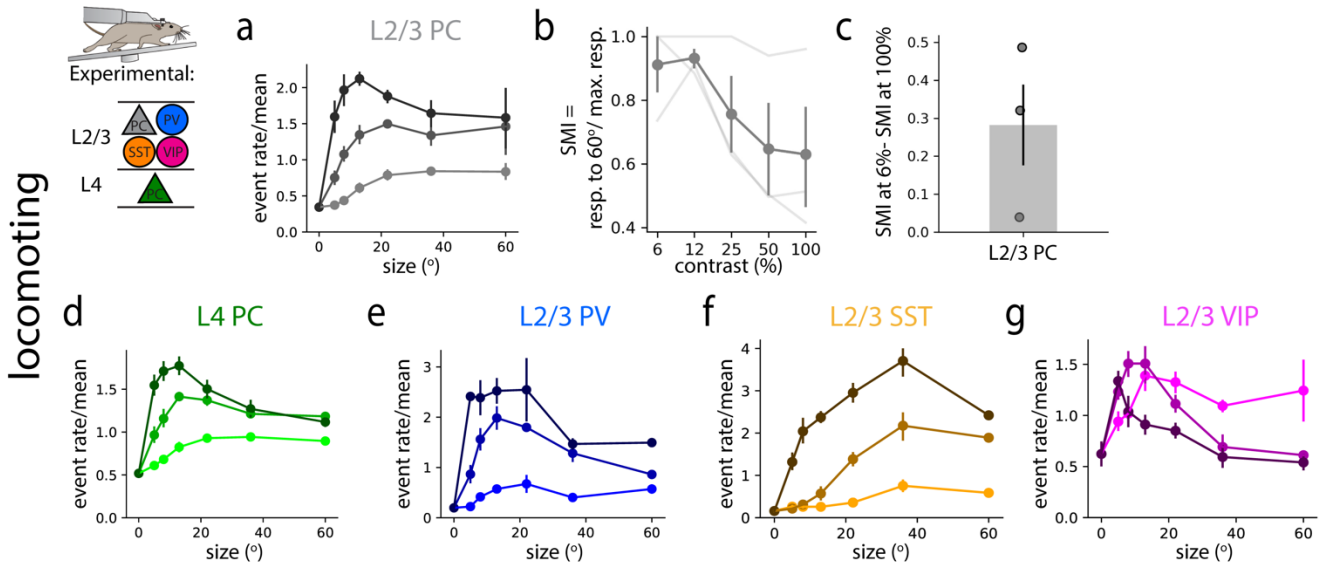

Figure S1. Similar cell-type specific responses to stimulus size and contrast during locomotion. A) Size tuning curves of L2/3 PCs in the locomoting condition, averaged across experiments. B) Surround modulation index (SMI; response to 60° size / response to preferred size) of L2/3 PCs as a function of contrast in the locomoting condition. C) Change in SMI between 6% and 100% contrast for all three cell types. **, significantly greater than 0, $p < 0.01$. D-G) Same as A), but for L4 PCs, L2/3 PV cells, L2/3 SST cells, and L2/3 VIP cells, respectively. Error bars indicate bootstrap SEM equivalent.

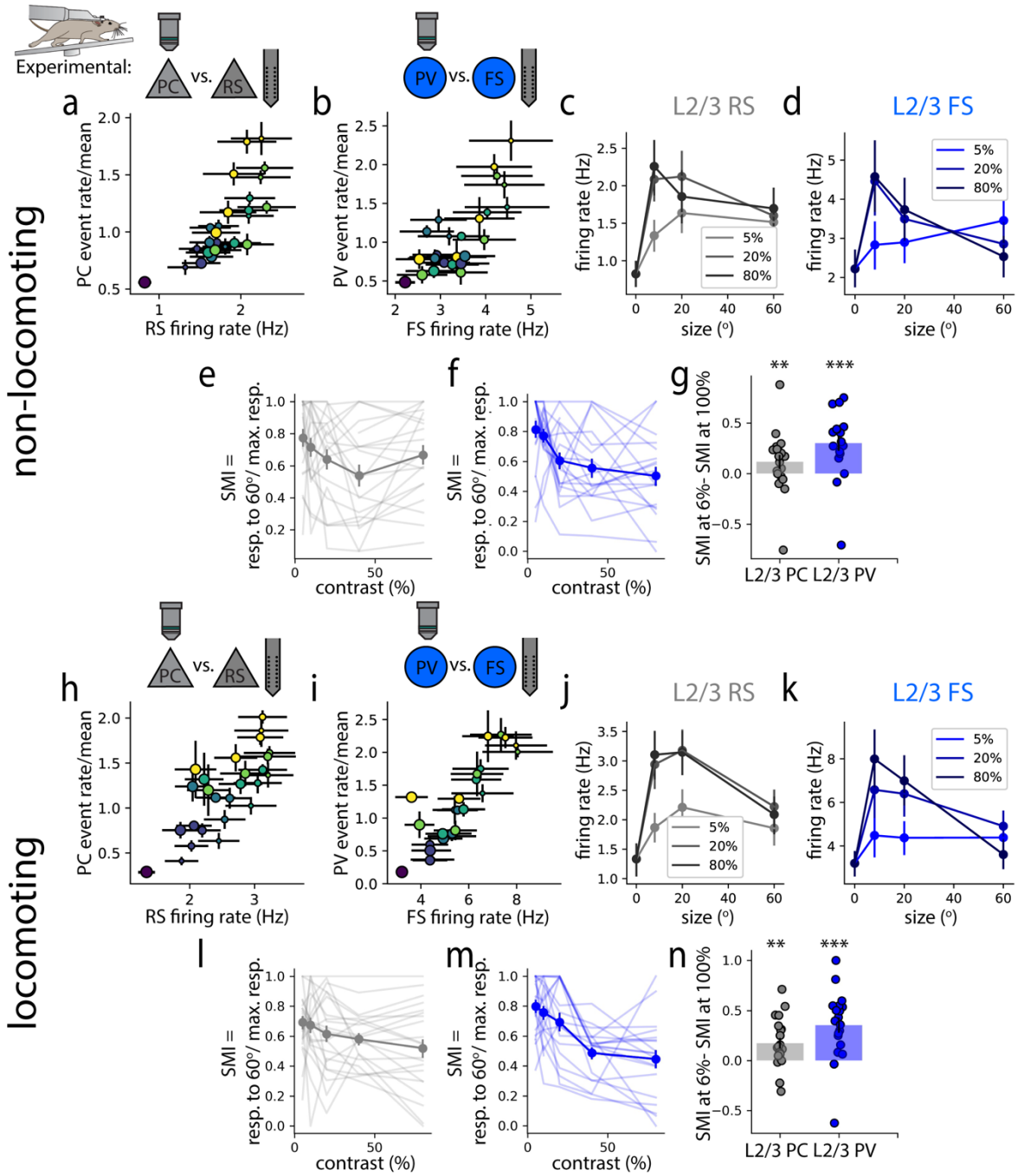

Figure S2. Extracellular electrophysiology reveals similar tuning properties as calcium imaging. A) Scatter plot of firing rate of regular spiking (RS) units recorded using extracellular electrophysiology, vs. PC event rate/mean across stimuli measured using calcium imaging for the equivalent stimuli, in the non-locomoting condition. Dot size and color are as in fig. 3A. B) Same as A), but for fast spiking (FS) units recorded using extracellular electrophysiology, vs. PV event rate/mean measured using calcium imaging. C) Size tuning curves, separated by contrast, for RS units plotted in A). D) Same as C) for FS units plotted in B). E) Surround modulation index

(SMI), defined as the response to 60° gratings divided by response to the preferred size gratings, as a function of contrast, for L2/3 RS units. Each line is a single recording session, and the bold line corresponds to average across recording sessions. F) same as E) for L2/3 FS units. G) Difference of SMI between 6% and 100% contrast. Each dot corresponds to one recording session. H-N) Same as A-G), for the locomoting condition. ** significantly positive, $p < 0.01$; ***, $p < 0.001$. Error bars indicate bootstrap SEM equivalent.

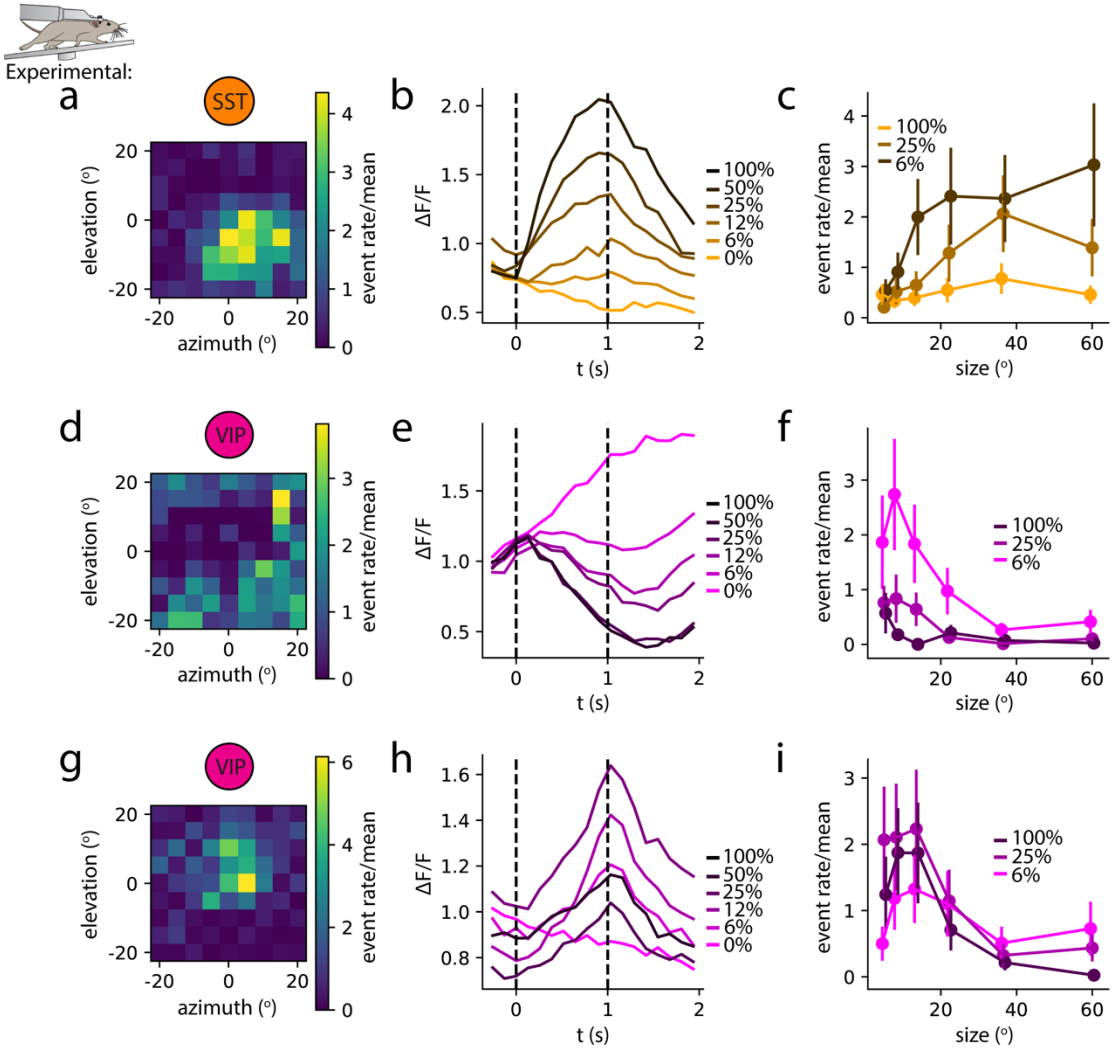

Figure S3. Example tuning curves show diversity of VIP cell size-contrast tuning. A) Receptive field of an example SST cell (see Methods). Mapped using 10° drifting gratings of time-varying direction, shown for 1.5 seconds each. B) ΔF/F time course of size-contrast responses for the neuron shown in A; each curve represents the response to gratings of a given contrast, averaged across sizes and orientations. C) Size tuning of the same cell, split up by contrast. D-F) Same as A-C), for an example contrast-suppressed VIP cell. G-I) Same as A-C), for an example contrast-facilitated VIP cell. Error bars indicate bootstrap SEM equivalent.

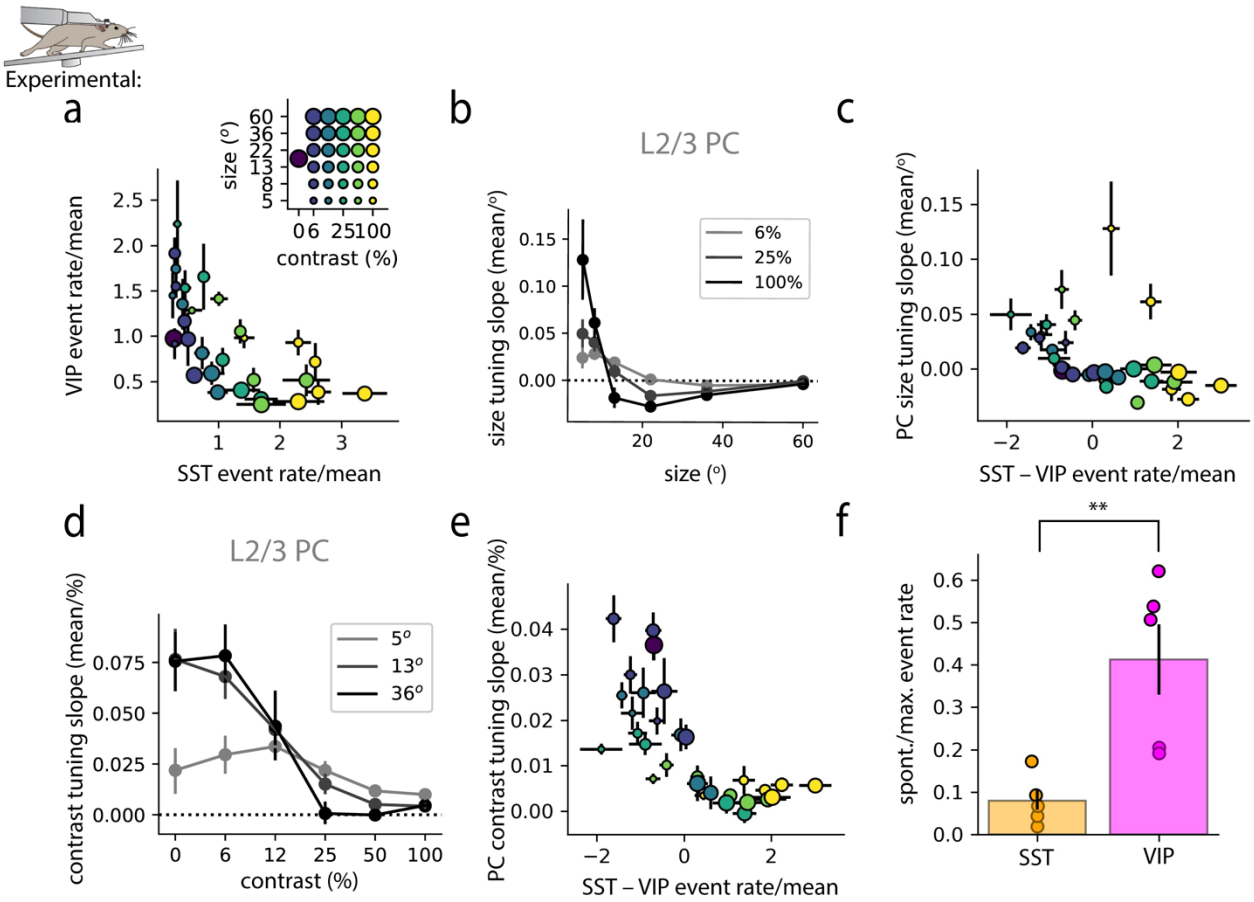

Figure S4. SST and VIP activity outline contrasting regimes of PC spatial integration. A) Average event rate of SST cells, normalized to the mean across stimuli, is plotted on the x axis, with VIP responses plotted on the y-axis, likewise normalized to the mean across stimuli. Dot size and color are as in fig. 3A. On the basis of their negative correlation, we define an axis based on the difference between SST and VIP activity. B) On the x axis is plotted size, and on the y axis is plotted the local slope of PC size tuning curves. Where the slope is positive, cells undergo surround facilitation on average, and where the slope is negative, cells experience surround suppression. C) PC size tuning slope is plotted against the difference of SST and VIP event rate. D) Same as B), but for the local slope of PC contrast tuning curves. E) Same as C), but with PC contrast tuning slope rather than size tuning slope. F) Spontaneous activity of SST and VIP cells, as a fraction of maximal sensory-evoked activity. ** significantly different, $p < 0.01$, Wilcoxon signed rank test. Error bars indicate bootstrap SEM equivalent.

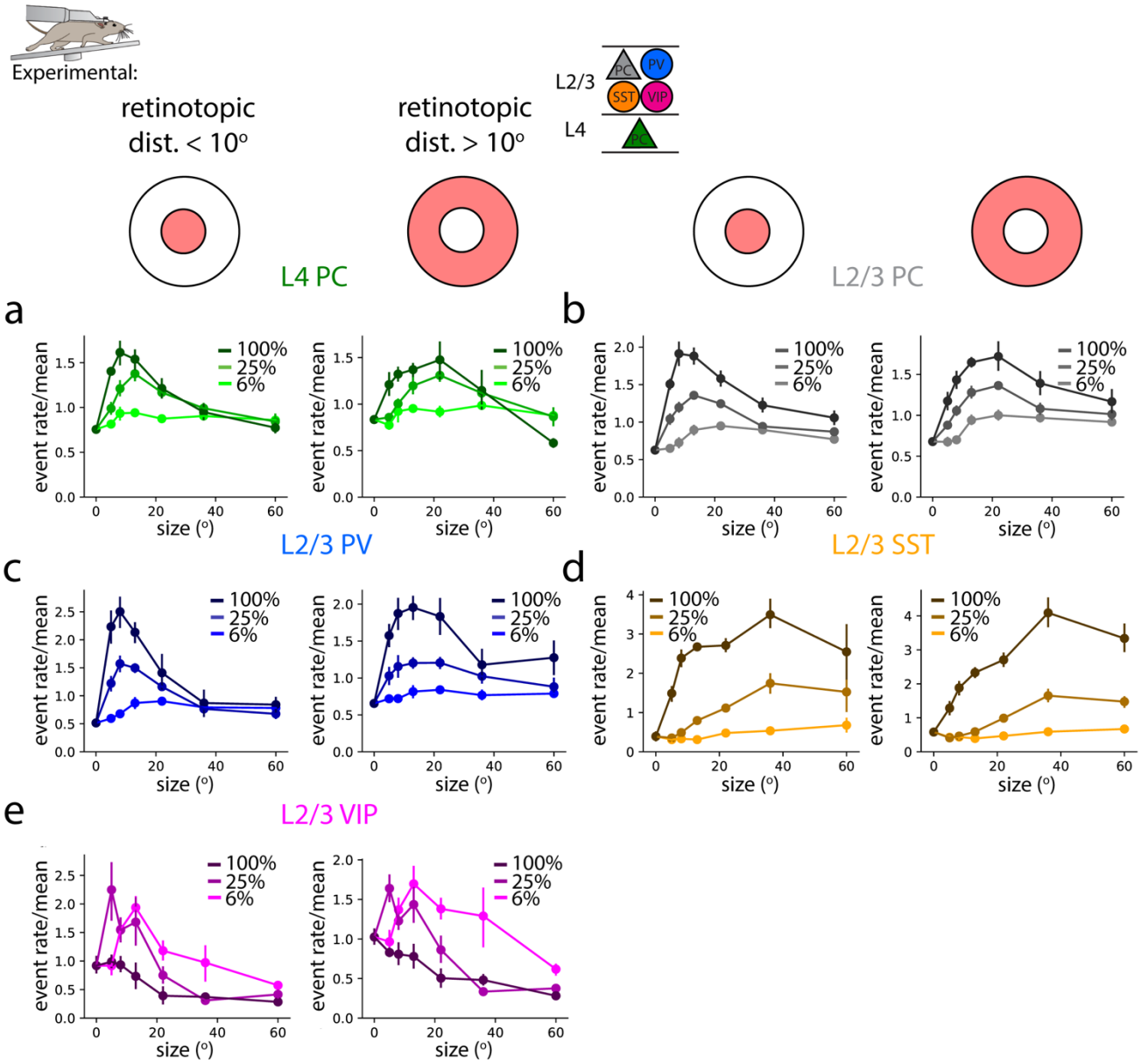

Figure S5. Neurons with receptive fields not aligned with the stimulus center show preference for larger sizes. A) Size tuning of L4 PCs, including only those located within 10 visual degrees of retinotopic space of the center of the stimulus representation (left). Beyond 10 visual degrees (right). B-E) Same as A), for L2/3 PCs, PV cells, SST cells, and VIP cells, respectively. Error bars indicate bootstrap SEM equivalent.

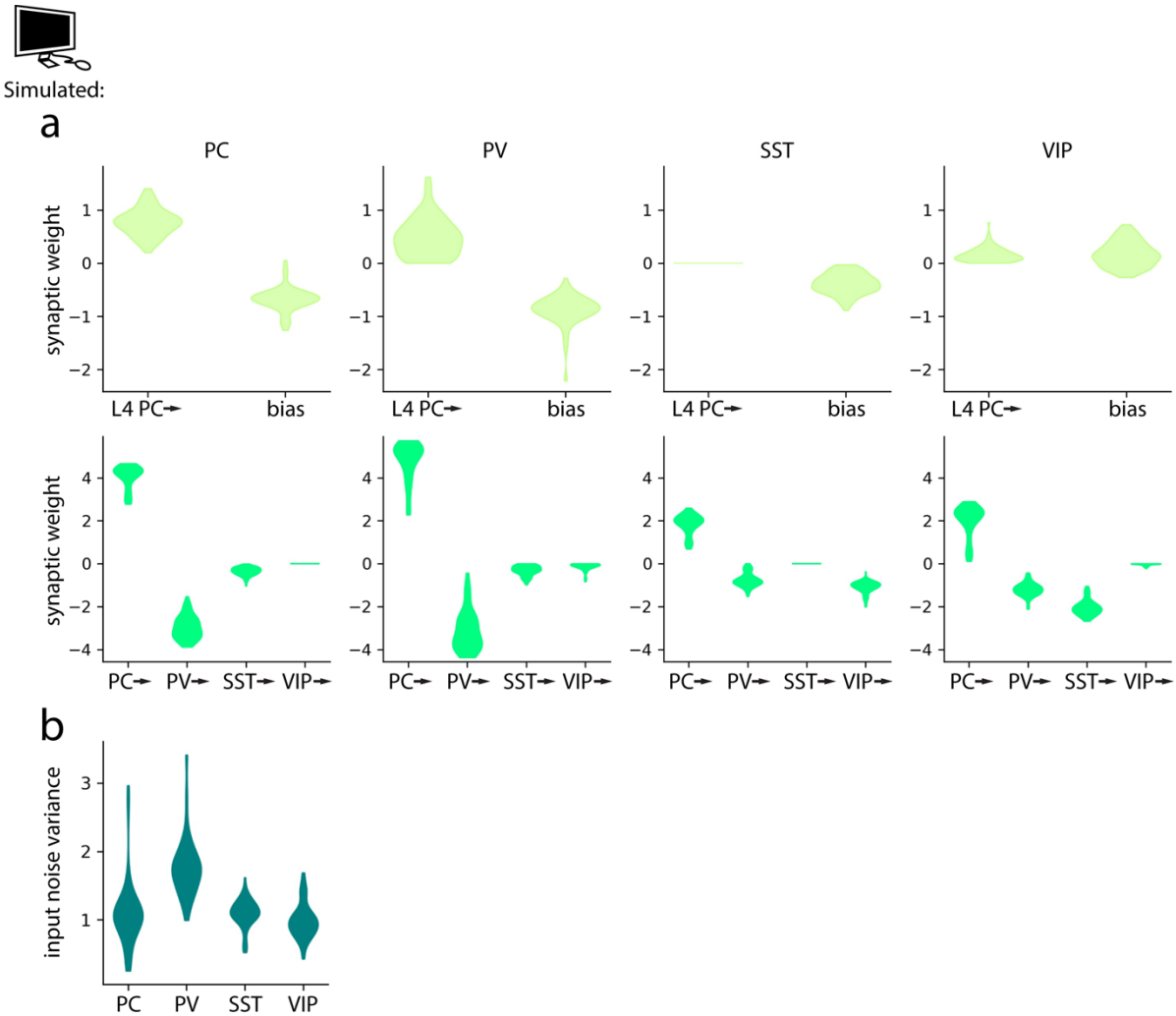

Figure S6. Well performing model fits show variability in fit parameters. A) Violin plots showing variability in synaptic input weights among model fits for each of the four L2/3 cell types modeled. B) Variance of intrinsic input noise for each cell type.

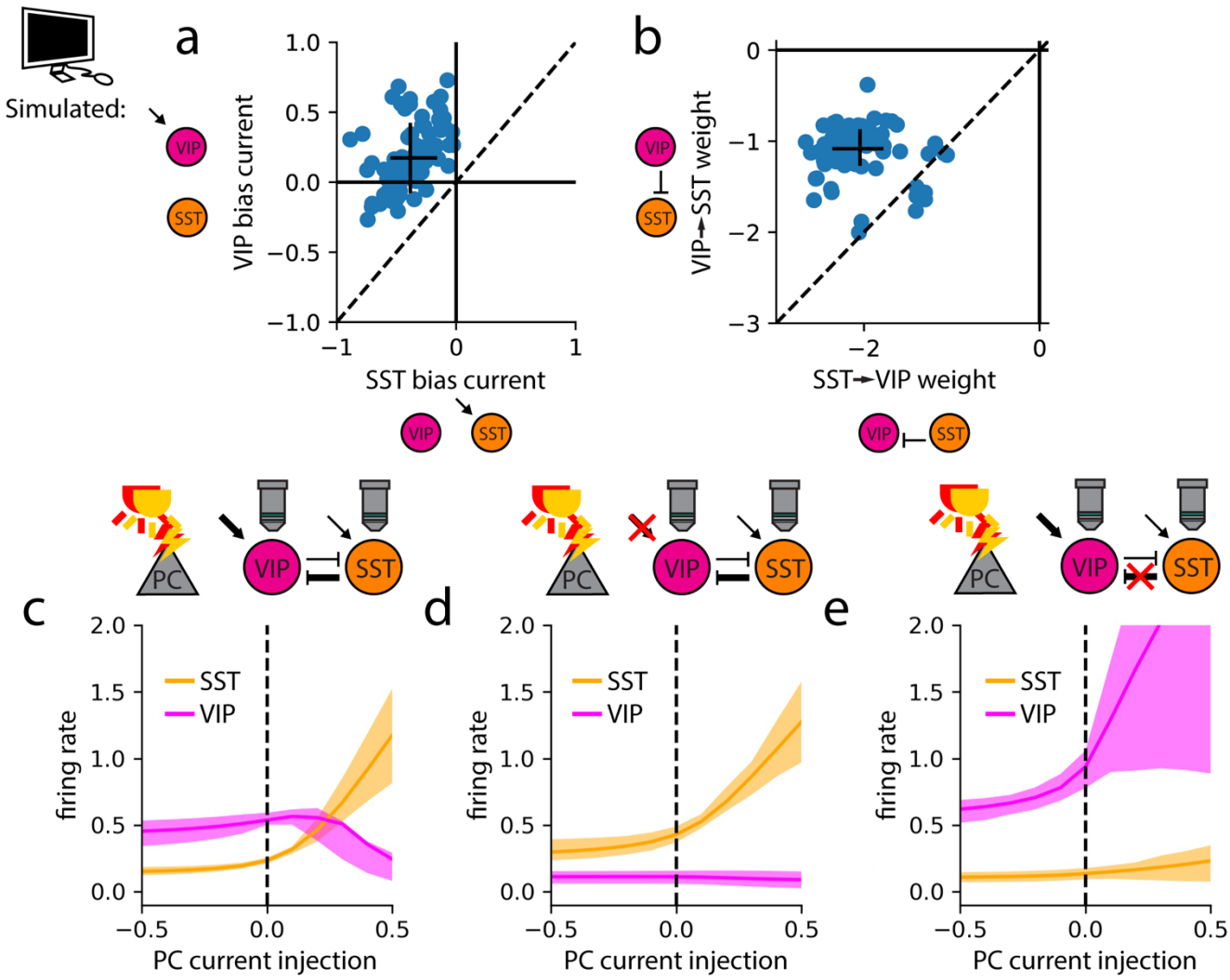

Figure S7. Network parameters support PC activity-dependent competition between VIP and SST cells. A) VIP bias current is plotted against SST bias current, for all successful model fits. VIP bias currents are significantly larger than SST bias currents, $p=8x10^{-16}$, Wilcoxon signed-rank test. B) VIP→SST weight is plotted against SST→VIP weight, across successful model fits. SST→VIP weights are significantly stronger (more negative) than VIP→SST weights, $p=4x10^{-15}$, Wilcoxon signed-rank test. C) Starting from the network steady state for 0% contrast (dashed line), positive or negative current injections to PCs are modeled, and the resulting steady state firing rates of SST and VIP cells are plotted as a function of injected current to PCs. D) Same as C), but after deleting (setting to 0) VIP bias current. E) Same as C), but after deleting SST→VIP weight. Shading indicates 16th to 84th percentile of model fits.

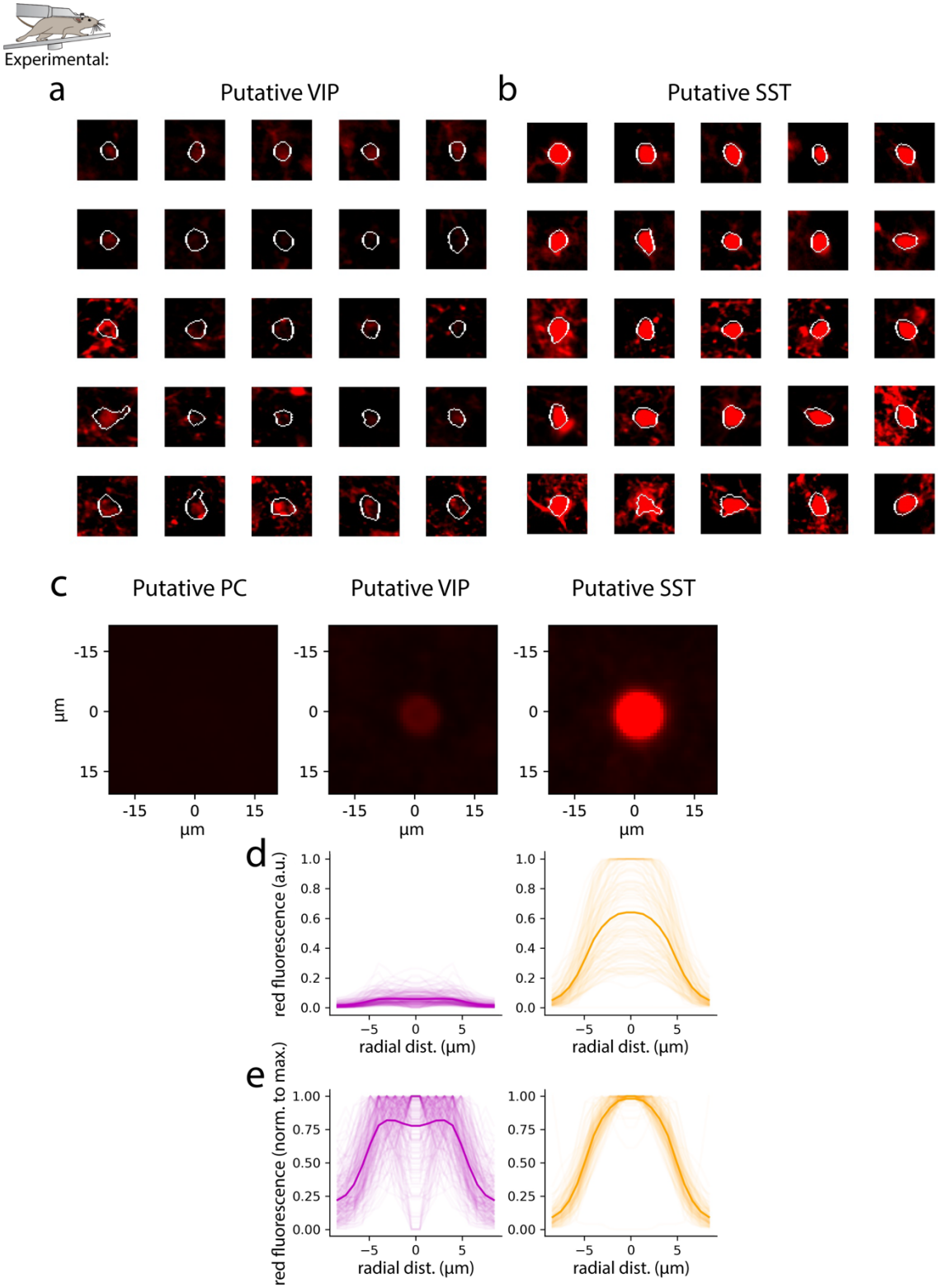
Experimental:
a
Putative VIP
b
Putative SST
c
Putative PC
Putative VIP
Putative SST
µm
-15
0
15
d
red fluorescence (a.u.)
radial dist. (µm)
e
red fluorescence (norm. to max.)
radial dist. (µm)

Figure S8. SST-tdTomato and VIP-mRuby3 cells can be distinguished by brightness and spatial profile. A) Outlines of putative VIP (membrane-bound mRuby3 expressing) cells, with red channel images. B) Analogous for putative SST (cytosolic tdTomato expressing) cells. C) Average red channel images for putative PCs (left), VIP cells (middle), and SST cells (right), aligned to the center of each cell. D) Red intensity (a.u.) as a function of radial distance from the center of the ROI. Each transparent line is one cell, and the bold line is the average. On the left, in magenta, are putative VIP cells, and on the right, in orange, are putative SST cells. E) Same plots as D), but normalized to the maximum value.

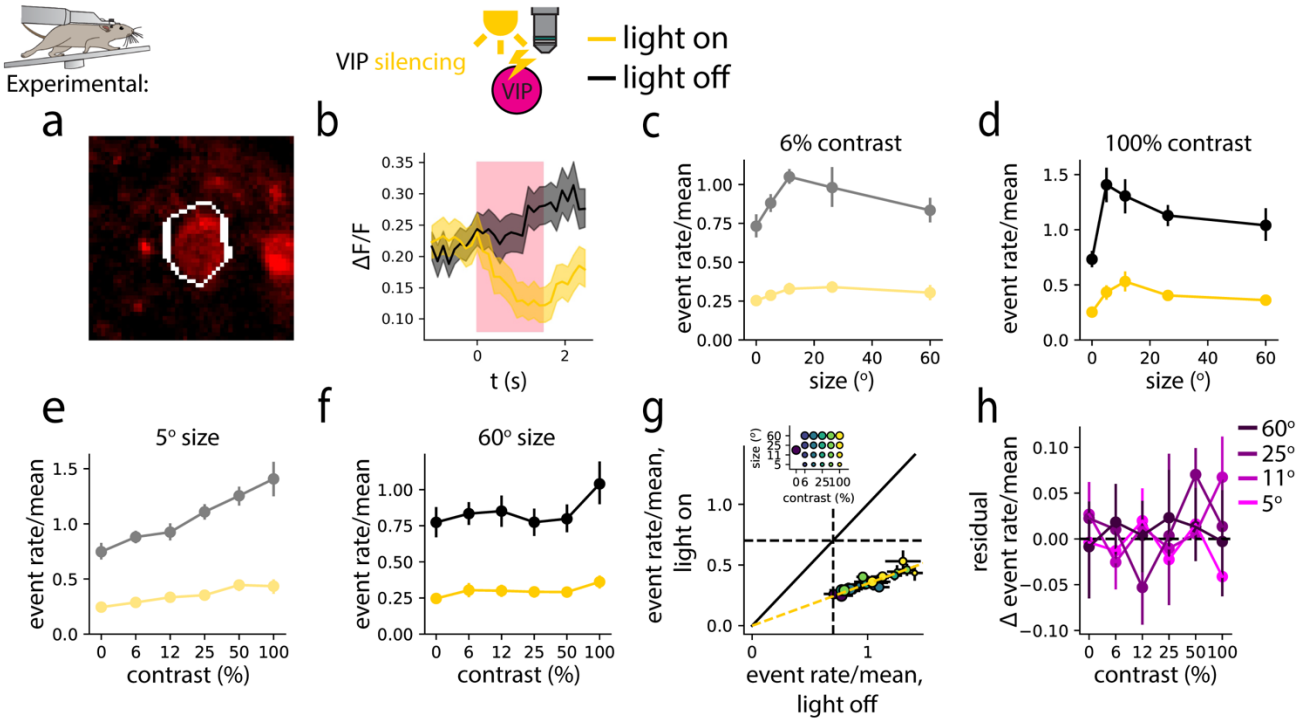

Figure S9. Optogenetic silencing of VIP cells. A) eNpHR3.0-mRuby3-labeled VIP cell from a VIP silencing experiment. B) ΔF/F averaged across all VIP cells, for gray screen trials following gray screen trials with no optogenetic stimulation. In yellow is the average trace for trials where the optogenetic stimulation light was on, and in black is the average trace for trials where the optogenetic stimulation light was off. C) Response of a VIP cell to gratings of varying size, at 6% contrast. In black is the light off response, and in yellow is the light on response. D) Same as B), for 100% contrast. E,F) Same as C), D), but for varying contrast, at 5° and 60° size, respectively. G) Scatter plot of light on vs. light off event rate for putative VIP cells at varying size and contrast. In yellow is the best fit line, with the intercept constrained to be 0. Dot size and color are as in fig. 3A. H) Residual effect of optogenetic manipulation not captured by the best fit line in G), for varying contrast, and at varying sizes. Shading and error bars represent bootstrap SEM equivalent.

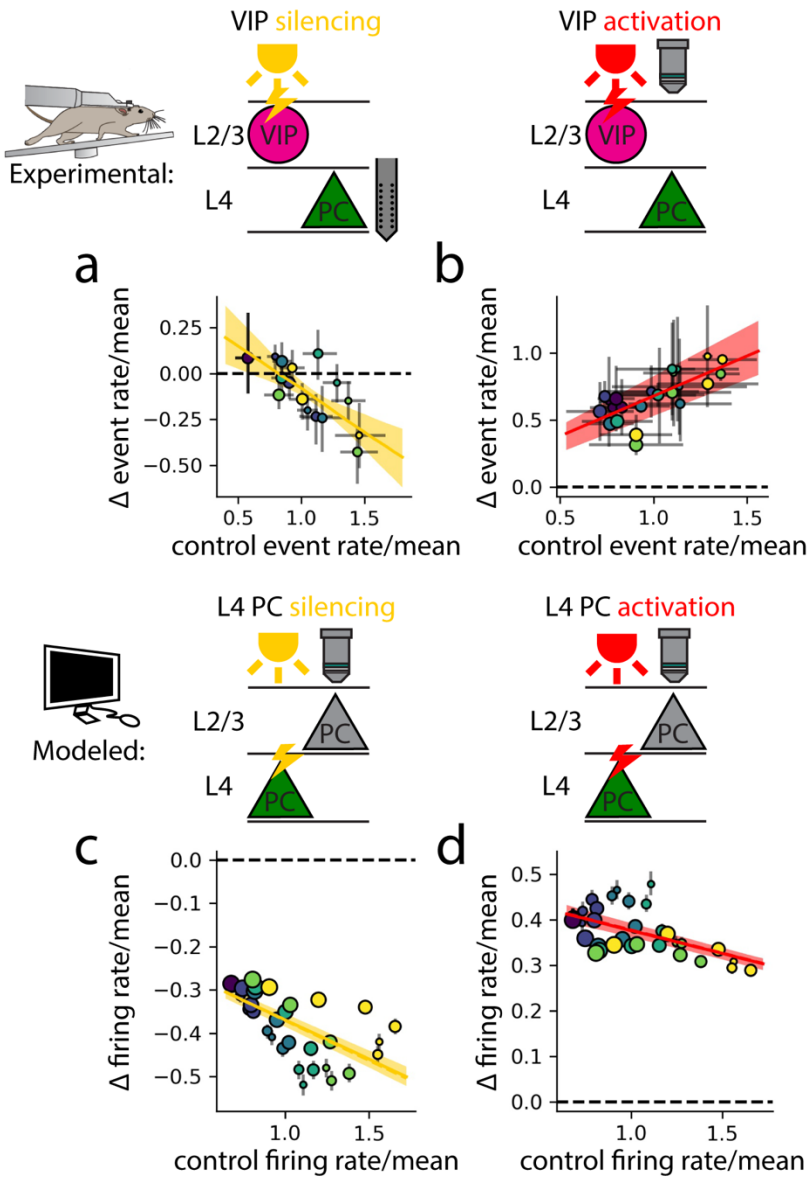

Figure S10. VIP manipulation modulates feedforward inputs to L2/3. A) Effect of VIP silencing on L4 regular spiking units measured using extracellular electrophysiology. Change in measured firing rate, normalized to mean light off firing rate, is plotted against light off firing rate, normalized to its mean, averaged across mice. Dot size and color are as in fig. 3A. B) Effect of VIP activation on L4 PCs measured using calcium imaging. Change in measured event rate, normalized to mean light off firing rate, is plotted against light off firing rate, normalized to its mean, averaged across mice. C) Response of L2/3 PCs to a modeled DC decrease in L4 PC firing rate across stimulus conditions. Change in firing rate, normalized to mean, is plotted against baseline firing rate. D) Same as C), but for a DC increase in L4 PC firing rate, across stimulus conditions. Error bars represent bootstrap SEM equivalent.

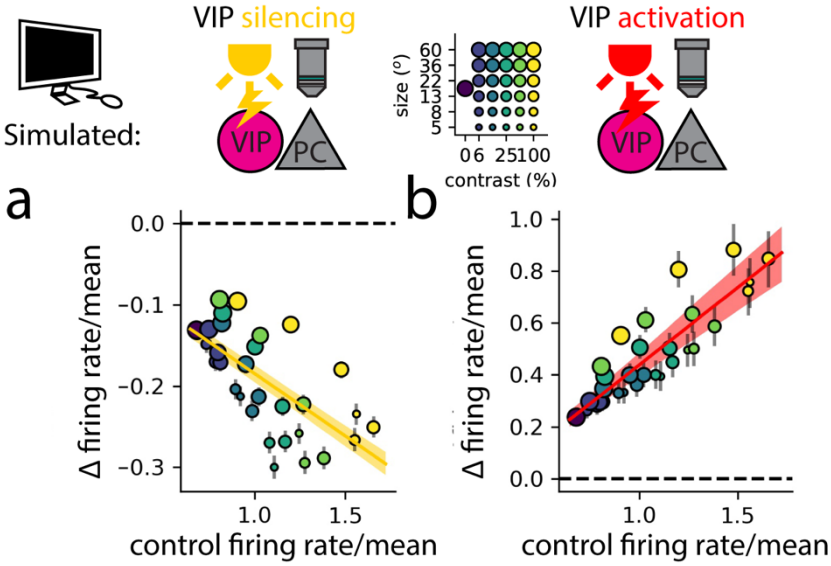

Figure S11. Modeled effect of bidirectional VIP manipulations depend on baseline activity, even without change to layer 4 activity. A) Scatter plot of modeled change in firing rate, vs. baseline firing rate, both normalized to mean across stimuli, in response to inhibitory current injection to VIP cells, without perturbing L4 PC activity. Dot size and color are as in fig. 3A. B) Same as A), but for excitatory current injection to VIP cells. Error bars represent bootstrap SEM equivalent.

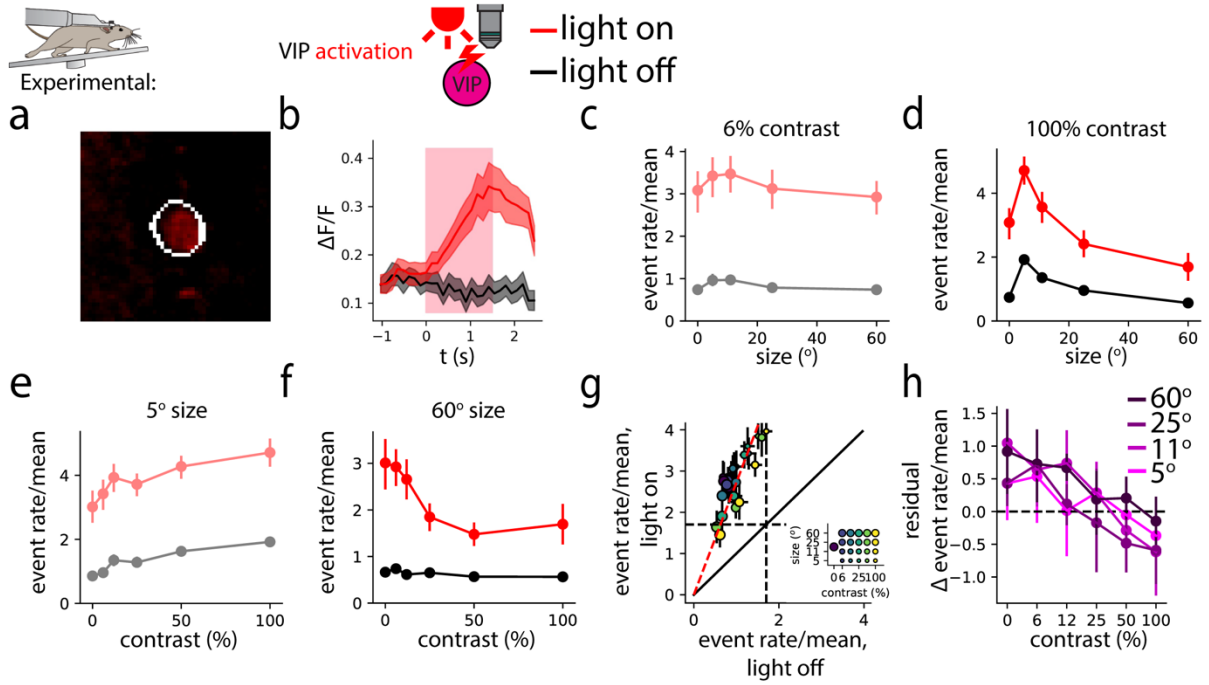

Figure S12. Optogenetic activation of VIP cells. A) ChrimsonR-tdTomato-labeled VIP cell from a VIP activation experiment. B) ΔF/F averaged across all VIP cells, for gray screen trials following gray screen trials with no optogenetic stimulation. In red is the average trace for trials where the optogenetic stimulation light was on, and in black is the average trace for trials where the optogenetic stimulation light was off. C) Response of VIP cells to gratings of varying size, at 6% contrast. In black is the light off response, and in red is the light on response. D) Same as B, for 100% contrast. E,F) Same as C), D), but for varying contrast, at 5° and 60° size, respectively. G) Scatter plot of light on vs. light off event rate for putative VIP cells at varying size and contrast. In red is the best fit line, with the intercept constrained to be 0. Dot size and color are as in fig. 3A. H) Residual effect of optogenetic manipulation not captured by the best fit line in G), for varying contrast, and at varying sizes. Shading and error bars represent bootstrap SEM equivalent.

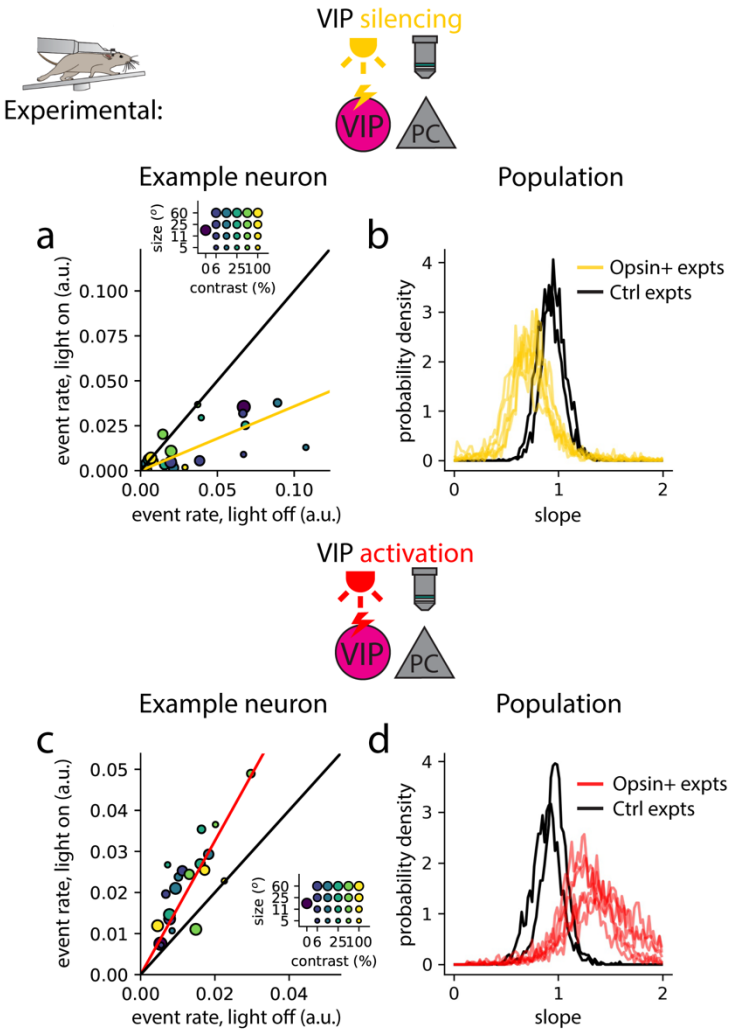

Figure S13. VIP perturbations bidirectionally control responses of VIP and non-VIP cells. A) Scatter plot of size-contrast tuning responses for an example neuron from a VIP-eNpHR3.0 expressing mouse. On the x-axis are plotted light-off responses, and on the y-axis, light-on responses. In yellow is the best-fit slope transforming light-off to light-on responses, and in black is the unity line (slope = 1). Dot size and color are as in fig. 3A. B) Histogram of best-fit slopes for optogenetic experiments (yellow) and control experiments (black) in which identical illumination parameters were used. Each line corresponds to one imaging session. C,D) Analogous to A), B) for VIP-ChrimsonR experiments, with optogenetic experiments represented in red, and control experiments in black.

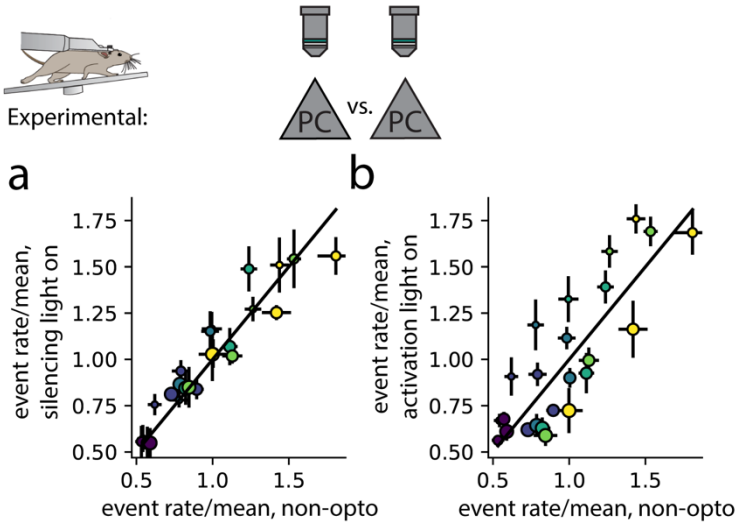

Figure S14. Measured baseline activity in calcium imaging and optogenetic experiments matches activity measured in only-calcium imaging experiments. A) Scatter plot of event rate, normalized to mean, for synapsin-GCaMP6s responses in VIP silencing experiments, with the optogenetic stimulation light off, vs. transgenic GCaMP6s responses of pyramidal cells in non-optogenetic experiments, for the analogous stimuli. Dot size and color are as in fig. 3A. B) Same as A), but for responses in VIP activation, rather than silencing, experiments. Error bars represent bootstrap SEM equivalent.

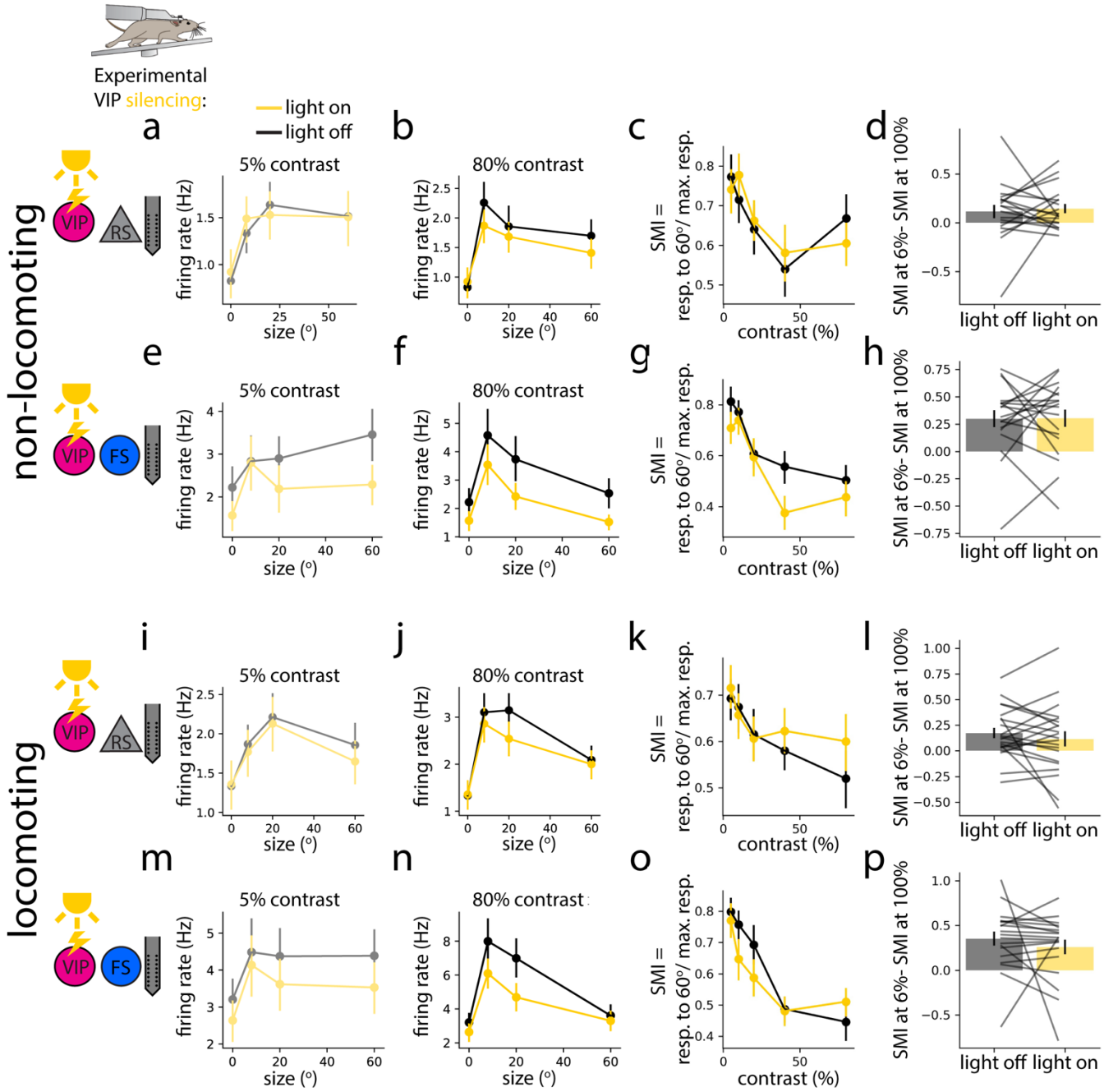

Figure S15. Extracellular electrophysiology confirms VIP silencing does not affect contrast dependence of surround suppression. A) Response of regular spiking (RS) units recorded using electrophysiology to drifting gratings of varying size, at 5% contrast, in the non-locomoting condition. B) Same as A, but at 80% contrast. C) Surround modulation index is plotted as a function of contrast, in the light on and light off case. D) Change in SMI between 6% and 100% contrast is plotted, for the light on and light off cases. Each line represents the average of units recorded over one experiment. E-H) Same as A-D), but for fast-spiking (FS) units. I-P) Same as A-

H), but for the locomoting condition. The light on and light off conditions are not significantly different in D), H), L), or P), $p > 0.05$. Error bars represent bootstrap SEM equivalent.

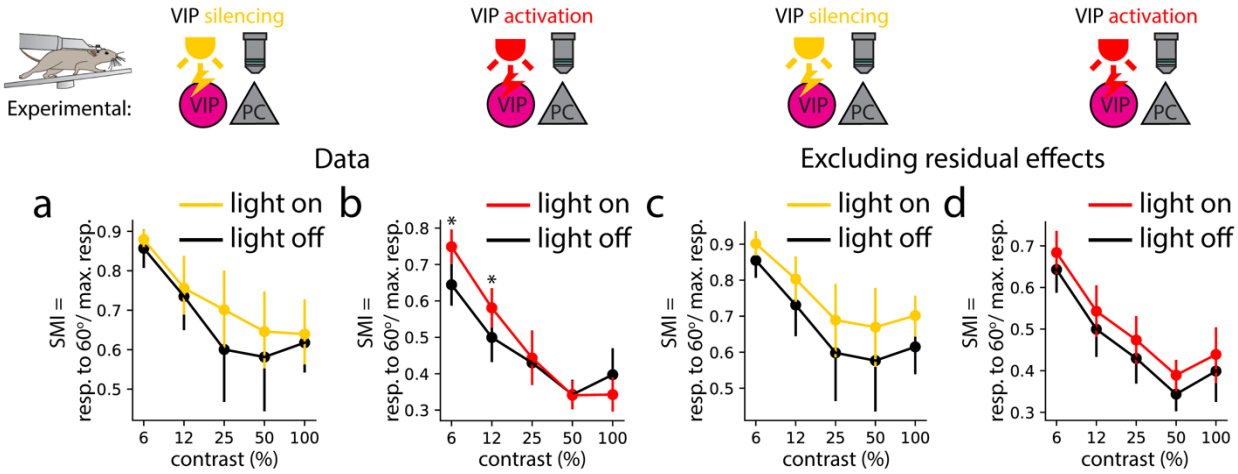

Figure S16. Linear firing rate transformations do not explain enhancement of contrast dependence of surround suppression. A,B) Fig. 5C,K are reproduced here for clarity. C) As in A), surround modulation index is plotted as a function of contrast, for the VIP silencing data. In black is the light off condition. In red is plotted, rather than the true light on condition, the prediction of a linear fit to the light on condition, based on the light off condition. D) Same as C), for the VIP silencing case. Error bars represent bootstrap SEM equivalent.

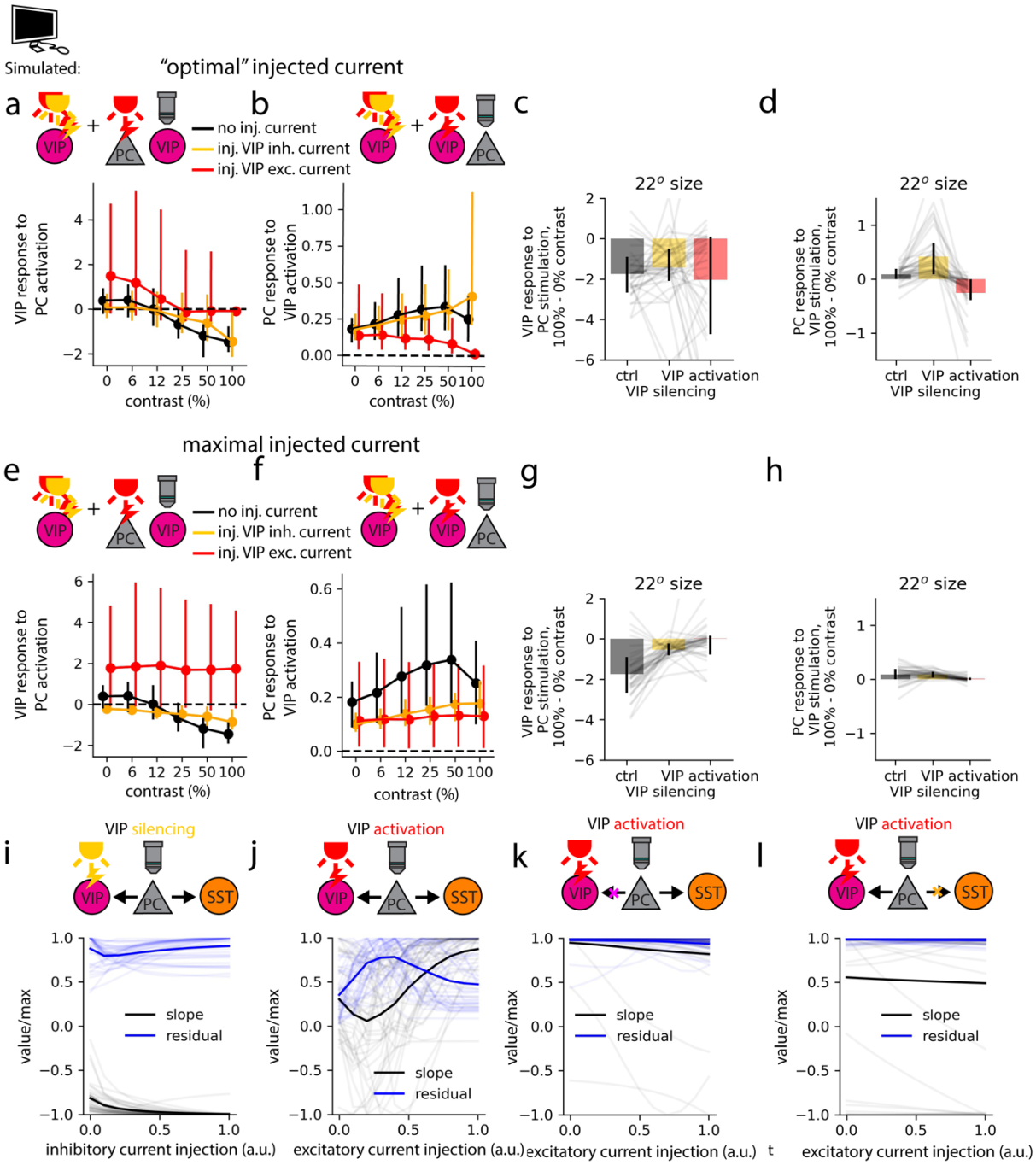

Figure S17. Positive PC-VIP feedback loop at low contrast is enhanced by intermediate levels of VIP activation, underlying asymmetric residual effects of VIP activation. A) Simulated response of VIP cells to small excitatory perturbations to PCs, as a function of contrast, at 22° size. Black curve corresponds to non-optogenetic condition. Yellow curve corresponds to simulated finite inhibitory current injection to VIP cells, along with empirically measured VIP silencing-dependent perturbation to L4 PCs. Red curve corresponds to simulated finite excitatory current injection to VIP cells, along with empirically measured VIP activation-dependent perturbation to L4 PCs. Current injection magnitudes are chosen to maximize average magnitude of residual effects of current injection. B) Same as A), but for PC responses

to small excitatory perturbations to VIP cells. C) Slope and average magnitude of residual of best fit line between baseline activity level and effect of optogenetic perturbation on PCs, for simulated finite inhibitory current injections to VIP cells of varying magnitude, along with (fixed) empirically measured VIP silencing-dependent perturbations to L4 PCs. D) Same as C), but for simulated finite excitatory current injections, along with (fixed) empirically measured VIP activation-dependent perturbations to L4 PCs. E,F) Same as C), D), but after deleting modeled PC→VIP weights. G,H) Same as C), D), but after deleting modeled PC→SST weights. I,J) Same as A), B), but with current injection magnitudes corresponding to the maximal injection magnitude plotted in C), D). Error bars represent 16th to 84th percentile of model fits.

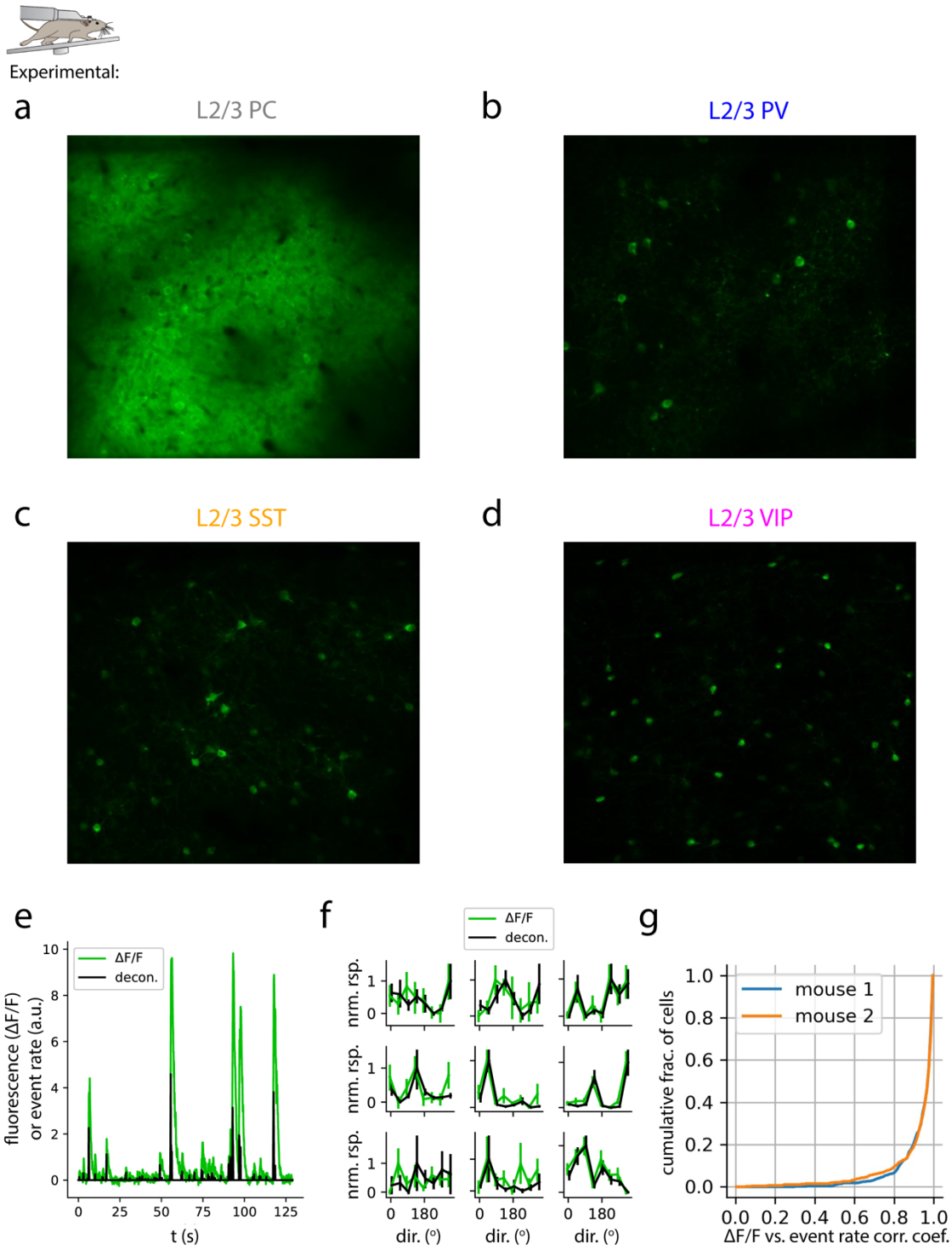

Figure S18. Example fields of view, and deconvolution analysis controls. A) An example imaging plane of a Camk2a-tTA; tetO-GCaMP6s animal, used for recording L2/3 PCs. Computed by averaging motion corrected frames across an experiment. B-D) Same as A), for PV-Cre; TITL2-GCaMP6s, SST-Cre; TITL2-GCaMP6s, and VIP-Cre; TITL2-GCaMP6s, respectively. E) Example

fluorescence (ΔF/F) trace with deconvolved event rate, from a L2/3 PC. Reproduced from fig. 1C. F) In a subset of control experiments, a longer inter-stimulus interval was used, so that evoked calcium transients did not overlap between successive trials. Orientation tuning in nine neurons with reliably estimated ΔF/F tuning curves (Pearson's $r > 0.5$ between halves of the data, see Methods) is plotted, as measured using ΔF/F and deconvolved event rate. Values are normalized for each to lie between 0 and 1. Error bars represent bootstrap SEM equivalents. G) Cumulative distribution of Pearson's r between ΔF/F and deconvolved tuning curves for two experiments (analyzing only neurons with reliably estimated ΔF/F tuning curves, n = 488/1131, 466/1060, respectively).

657 **Methods**
658
659 **Experimental model details**
660
661 All experiments were performed on mice between 1.5 to 14 months of age. CaMKII-tTA mice
662 (RRID:IMSR_JAX:003010) crossed to tetO-GCaMP6s mice (RRID:IMSR_JAX:024742) were used
663 when imaging L2/3 pyramidal cells. Both lines had been outcrossed to the ICR line (Charles
664 River) for several generations. These mice were on a mixed background between outcrossed
665 tetO-GCaMP and camk2-tTA on the C57/B6 background. For L4 PC experiments (resp. L2/3 SST,
666 L2/3 VIP, and L2/3 PV experiments), Scnn1a-Tg3-Cre (resp. Sst-IRES-Cre, Vip-IRES-Cre, and Pv-
667 IRES-Cre) mice were crossed to Ai162(TIT2L-GC6s-ICL-tTA2)-D mice (RRID:IMSR_JAX:031562).
668 For VIP optogenetic and calcium imaging experiments, Vip-IRES-Cre or Vip-IRES-Cre crossed to
669 Sst-IRES-Flp were used. For optogenetic and electrophysiology experiments, Vip-IRES-Cre or Sst-
670 IRES-Cre animals were used. Both female and male animals were used, and maintained on a
671 12:12 reversed light:dark cycle. All procedures were approved by the Animal Care and Use
672 Committee of UC Berkeley.
673
674 **Preparation for *in vivo* two photon imaging**
675
676 Headplate attachment, habituation to running on a circular treadmill, and cranial window
677 installation were performed as described previously (Lyall et al. 2020). Briefly, anesthesia was
678 induced with 5% isoflurane and maintained at 1-3% during surgery. Respiratory rate and
679 response to toe/tail pinching was monitored throughout surgery to ensure adequate anesthetic
680 depth. 0.05 mg/kg of buprenorphine was administered subcutaneously for post-operative
681 analgesia, and 2 mg/kg of dexamethasone as an anti-inflammatory. The scalp was disinfected
682 with 70% alcohol and 5% iodine. The skin and fascia above the sensory cortices were removed
683 and Vetbond (3M) was applied to the skull surface and wound margins. A custom titanium
684 headplate was fixed to the skull with dental cement (Metabond). A cranial window was
685 installed to provide for optical access to the cortex. A biopsy punch was used to create a 3.5mm
686 diameter craniotomy over the left primary visual cortex. A window plug consisting of two 3 mm
687 diameter coverslips glued to the bottom of a single 5 mm diameter coverslip using Norland
688 Optical Adhesive #71 was placed over the craniotomy and sealed permanently using dental
689 cement (Orthojet or Metabond). The dental cement was coated in a layer of black oxide to
690 mitigate light leakage during subsequent experiments. Mice were provided at least two days to
691 recover.
692 For VIP silencing experiments, neonatal Vip-IRES-Cre; Sst-IRES-Flp (P4–6) were briefly
693 cryo-anesthetized and placed in a head mold. Transcranial injection of ~45nl of undiluted AAV9-
694 CAG-DIO-eNpHR3.0-mRuby3 (UPenn Vector Core) was performed using a Drummond Nanoject
695 injector at three locations in left V1 using a glass pipette beveled to fine tip (~30–60µm). With
696 respect to the lambda suture coordinates for V1 were 0.0 mm AP, 2.2 mm L and injection was
697 as superficial as possible under the skull.
698 For VIP activation experiments, Vip-IRES-Cre mice were injected with AAV9-syn-
699 GCaMP6s (UPenn Vector Core) and rAAV9-syn-DIO-ChrimsonR-tdT (UNC Vector Core) virus in

700 left V1. For VIP silencing experiments, Vip-IRES-Cre; Sst-IRES-Flp mice were injected with AAV9-
701 syn-GCaMP6s (UPenn Vector Core) virus in left V1. Briefly, they were anesthetized and
702 administered buprenorphine as described above. A dental drill (Foredom) was used to create a
703 small burr hole 2.75 mm lateral to bregma. Then a WPI UltraMicroPump3 injector was used to
704 inject 300-400 nL of the virus at a rate of 50 nL/min. Post-injection, the needle was left in the
705 brain for 5 minutes to allow the viral solution to absorb into the tissue. Injected mice were
706 provided 2-3 weeks with intermittent head-fixation over the circular treadmill to allow the
707 infected neurons to ramp up expression of GCaMP6s.
708
709 **Visual stimulus presentation, *in vivo* imaging, and pupil tracking**
710
711 For visual stimulus presentation, the monitor was placed 13-15 cm from the eye. Animals were
712 habituated to visual stimulation on the setup for at least two sessions prior to imaging. Before
713 and/or after each experiment, receptive fields were mapped using 10° drifting grating patches.
714 These patches had spatial frequency of 0.08 cycles per degree, and a temporal frequency of 1
715 Hz, with direction cycling through $0\text{-}360^o$ over the course of 1.5 seconds. They appeared at
716 randomly interleaved locations tiling a 40 x 40 visual degree grid, sampled at 5° intervals, with
717 1.5 second inter-stimulus intervals. In subsequent size-contrast experiments, the visual stimulus
718 consisted of square wave drifting gratings, with directions tiling 0-360 degrees at 45° intervals,
719 with a spatial frequency of 0.08 cycles per degree, and a temporal frequency of 1 Hz (calcium
720 imaging experiments without optogenetics) or 2 Hz (calcium imaging and optogenetic
721 experiments). Visual stimulus presentation lasted one second, followed by a one second inter-
722 stimulus interval. Patch configurations, orientations, and sizes were pseudorandomly
723 interleaved, and stimuli were generated and presented using the Psychophysics Toolbox
724 (Brainard, 1997). Each distinct visual stimulus was displayed for 5-10 repetitions.
725 Mice were head-fixed on a freely spinning running wheel under a Nixon 16x-
726 magnification water immersion objective and imaged with a two-photon resonant scanning
727 microscope (Neurolabware) within a light tight box. The imaging FOV was 430 by 670 um, with
728 four planes spaced 37.5 µm apart imaged sequentially using an electrotunable lens (Optotune),
729 sampling each plane at an effective frame rate of 7.72 Hz. For L2/3 imaging, imaging depth was
730 100 – 300 µm, and for L4 imaging, depth was 350 – 500 µm deep. Electrical tape was applied
731 between the objective and the mouse's headplate to block monitor light from entering the
732 microscope.
733 Locomotion was monitored using a rotary encoder, with trials where mean absolute run
734 velocity > 1 cm/sec classified as "locomoting" and < 1 cm/sec classified as "non-locomoting".
735 Eye movements were imaged using a Basler Ace aCA1300-200um camera, with a hot mirror
736 (Edmund Optics) placed between the eye and the monitor reflecting infrared light for eye
737 imaging while transmitting visible light for visual stimulation. Infrared illumination was provided
738 by the two photon imaging laser, transmitted through the pupils, as well as a panel of 850nm
739 LEDs (CMVision). Pupil location and diameter were tracked using custom MATLAB code.
740
741 **Imaging and optogenetic stimulation**
742

743 Optogenetic stimulation through the objective was performed with a 617 nm LED (Thorlabs),
744 filtered through a 632/22 nm single-band bandpass filter (Semrock), at an amplitude through
745 the objective of either 6 mW (VIP silencing experiments) or 1.5 mW (VIP activation
746 experiments). Electrical tape between the mouse's head and the objective served to mitigate
747 direct visual stimulation by the optogenetic light. The PMT was not gated, but protected by a
748 strict shortpass filter. Optogenetic illumination began 0.25 seconds prior to visual stimulus
749 delivery, and ended 0.25 seconds after. Small square wave optogenetic artifacts visible on the
750 PMT were subtracted in post-processing.
751
752 **Calcium imaging analysis**
753
754 Motion correction and ROI segmentation was performed using Suite2p (Pachitariu et al. 2017).
755 Neuropil subtraction was applied as described in (Lyall et al., 2020). ΔF/F traces were
756 calculated as

757 $$\Delta F/F = \frac{F(t) - F_0}{F_0}$$

758 with baseline F_0 computed over a sliding 20th percentile filter of width 3000 frames. Because
759 the inter-stimulus interval was reduced in V1 recordings to permit more stimuli to be displayed,
760 calcium transients overlapped between successive trials. Therefore, we deconvolved calcium
761 traces for this data using OASIS with L1 sparsity penalty (Friedrich et. al., 2017), using ΔF/F
762 traces as input.
763 To confirm that the deconvolution procedure did not distort tuning curve
764 measurements, we performed two experiments with longer inter-stimulus intervals (3 seconds
765 rather than 1 second), varying only stimulus direction, at fixed 15° size and 100% contrast, for
766 20-30 trials per condition. Because evoked calcium transients did not overlap between
767 successive trials in this condition, tuning curves computed using ΔF/F and deconvolved event
768 rate should agree quantitatively (Fig. S18f). To restrict our analysis to neurons for which our
769 estimate of the tuning curve with ΔF/F was robust (e.g. neurons that were visually responsive
770 and orientation-tuned) we randomly split trials into two halves, computed tuning curves for
771 each half, and computed Pearson's correlation coefficients between the two independent
772 tuning curve estimates. We determined that a neuron's tuning curve measurement was robust
773 if the two estimates were correlated with $r > 0.5$ ($n = 488/1131$, $466/1060$ for the two
774 experiments). For these neurons, we then computed tuning curves based on all trials, using
775 ΔF/F and deconvolved event rates. Indeed, we found that for both mice, ΔF/F and deconvolved
776 estimates of tuning curves were correlated with $r > 0.9$ in ~80% of neurons.
777
778 **Retinotopic map estimation**
779
780 Responses to receptive field mapping stimuli were fit using 2D gaussians. The underlying
781 retinotopic map was estimated using linear regression of cell centers (in microns of cortical
782 space) vs. receptive field centers (in degrees of visual space). For subsequent analyses, neurons
783 were separated based on either their receptive field center relative to the center of the size-
784 contrast stimulus, or based on their location on the estimated retinotopic map, relative to the
785 center of the stimulus representation, as indicated in the text. For each FOV, the retinotopic

786 map orientation relative to the rostral-caudal and medial-lateral axes, and cortical
787 magnification, was confirmed to be consistent with V1.
788
789 **Simultaneous imaging of VIP and SST activity using Cre-Flp**
790
791 We used VIP-Cre SST-Flp mice, injected with GCaMP6s expressed in all neurons. SST cells
792 expressed cytosolic tdTomato in a Flp-dependent manner, while VIP cells expressed Cre-
793 dependent mRuby3 fused to eNpHR3.0. Using calcium imaging, we identified SST cells using
794 their bright, cytosolic red signal, compared with the dimmer, membrane bound mRuby3 in VIP
795 cells; they could be distinguished both by membrane localization and brightness of the red
796 fluorophore (fig. S8).
797
798 **Recurrent network model**
799
800 For a detailed expanation, see Supplementary Note. Briefly, we modeled cortical space using
801 two spatial domains. The first represented neurons within ten visual degrees of retinotopic
802 space of the stimulus representation's center; the second, neurons beyond 10 degrees. Activity
803 in layer 4 pyramidal cells (L4 PCs) in each spatial domain was treated as input to the four
804 recurrently connected layer 2/3 (L2/3) populations in each pixel. The full weight matrix
805 describing synaptic connections between the four L2/3 cell types in each of the two spatial
806 domains was modeled as the product of a cell type-dependent term, describing the connection
807 strength of cell type *I* onto cell type *j*, multiplied by a term describing the integration across
808 space, and a term describing integration across orientations, of the postsynaptic population *j*.
809 Thus, the full 8x8 matrix of recurrent synaptic connections was described by a 4x4 matrix, plus a
810 4-dimensional vector. A similar procedure was used to generate the full 2x8 matrix of
811 feedforward synaptic connections from L4 PCs. A four-dimensional vector gave the bias current
812 for each L2/3 population. The linear combination representing synaptic input currents was then
813 passed through a distinct static nonlinearity for each cell type. The shape of this nonlinearity
814 was determined by the intrinsic variability in a given cell type's input current, which was fit for
815 each cell type.
816 Because ***r*** appears on both the left and right sides of equation (1), we say that solutions
817 for ***r*** must in general be "self-consistent." For each cell population and each stimulus condition,
818 a stimulus-dependent residual current parameter was introduced, added to the synaptic input
819 and bias currents, so that perfect self-consistency was not required at each step of the
820 optimization. However, squared error penalties on these residual currents ensured that the
821 final network parameters achieved nearly perfect self-consistency. The model fits were
822 randomly initialized, and optimized using L-BFGS. The cost function incorporated both the
823 calcium imaging data for all cell types, and the optogenetic silencing data (combining both
824 calcium imaging and electrophysiology results). The optogenetic data were fit by linearizing the
825 model around the firing rates in the unperturbed condition. Several synaptic weights (L4
826 PC→SST, SST→SST, and VIP→PC) were constrained to be 0, and the PC→PC weight was
827 constrained to be large, in the sense that the product $w_{PC\text{->}PC}\,\varphi_{PC} > 1$, in units where the synaptic
828 leak current is 1, for every stimulus condition (with φ_{PC} as defined below).

For steady state solutions to equation (1), the change in firing rate r expected from a small change in input current I can be computed as the product

$$\Delta r \approx \varphi \Delta I, (2)$$

where φ is the slope of the firing rate nonlinearity around the steady state solution $\boldsymbol{r}$. Because I is itself a function of $\boldsymbol{r}$, we were able to simulate the response of a cell population j to small current injections to population j by computing a "response matrix" R as in (Del Molino et al., 2017):

$$\Delta \mathrm{r} = (1 - \Phi W)^{-1} \Phi \Delta h = R \Delta h. (3)$$

This amounts to linearizing $\boldsymbol{r}$ about a steady state solution to equation (1). Here, $\boldsymbol{\Delta h}$ is a vector of optogenetically induced currents, and Φ is a diagonal matrix whose entries are the values of φ for each cell type. The matrix R yields the theoretical prediction for the effect of small current injections to a given cell population j, on any cell population i. This matrix changes as a function of stimulus via changes in $\boldsymbol{r}$, and thus φ for each cell type.

We leveraged these recurrent network model fits to predict the effects of manipulations on network activity, some experimentally realizable with current technology, and some not. First, we simulated the deletion of certain synaptic connections. For these simulations, we allowed the network to evolve to a new steady state according to equation (1), after setting certain elements of the 4x4 L2/3 synaptic weight matrix to 0, with all other parameters held constant. Second, we simulated the injection of inhibitory (negative) or excitatory (positive) current to specific cell types, modeled as a stimulus-dependent DC offset to the synaptic input current for that cell type. Again, we allowed the network to evolve to a new steady state according to equation (1). In both of these cases, we computed both the perturbed steady state firing rates $\boldsymbol{r}$, as well as the perturbed response matrix R, resulting from the perturbed values for Φ and W.

For simulations of optogenetic silencing and activation of VIP cells, we tuned the magnitude of current injection for each model fit based on the computed response matrix. In particular, for both silencing and activation simulations, we chose current magnitude to maximize the dynamic range of the term corresponding to PC cooperation or competition across space ($R_{near\ PC,\ far\ PC}$), defined as the absolute difference between the maximum and minimum values of $R_{near\ PC,\ far\ PC}$ across stimuli.

Quantification and statistical analysis

Statistically significant differences between conditions were determined using standard nonparametric tests in the SciPy library, including the Wilcoxon signed-rank test and Mann-Whitney U test. Analyses were performed on each ROI's deconvolved event rate for each trial. A single trial's response was calculated as the average deconvolved event rate during the entire 1 second of stimulation. 95% confidence intervals and SEM equivalents (68% confidence intervals) were generated via bootstrap. For validation of the deconvolution procedure, trials were split randomly into two halves, and tuning curves were computed on each half of trials. Neurons whose tuning curves computed on both halves of the data using ΔF/F agreed with Pearson's r>0.5 were retained. For these neurons, tuning curves were computed across all trials using both ΔF/F and deconvolved event rate (fig. S18f,g).

Data Availability

The data that support the findings of this study are available from the corresponding author upon reasonable request.

Contributions

D.P.M., J.V., A.P., K.D.M., and H.A. conceived the study. D.P.M. performed the calcium imaging experiments. J.V. performed the extracellular electrophysiology experiments. D.P.M. designed and built the recurrent network model, and designed and carried out *in silico* experiments. D.P.M. and H.A. wrote the paper, with input from all other authors.

Acknowledgements

The authors acknowledge the GENIE Project, Janelia Farm Research Campus, and the Howard Hughes Medical Institute for the GCaMP6 viruses. Thanks to the members of the Adesnik Lab, particularly Hayley Bounds, Mora Ogando, and Hyeyoung Shin for helpful comments. Thanks also to Charles G. Frye, Sang Min Han, and Benjamin E. Smith. D.P.M. was supported by an NSF Graduate Research Fellowship. A.P. would like to acknowledge the support of the Swartz Foundation Fellowship for Theory in Neuroscience 2019-4 and 2020-6. H.A. is a New York Stem Cell Foundation-Robertson Investigator. This work was supported by The New York Stem Cell Foundation. This work was supported by NEI grant R01EY023756-01 and U19NS97613.

BIBLIOGRAPHY

Abs, Elisabeth, Rogier B. Poorthuis, Daniella Apelblat, Karzan Muhammad, M. Belen Pardi, Leona Enke, Dahlia Kushinsky, et al. 2018. "Learning-related plasticity in dendrite-targeting layer 1 interneurons." *Neuron* (Elsevier) 100: 684–699.

Adesnik, Hillel, William Bruns, Hiroki Taniguchi, Z. Josh Huang, and Massimo Scanziani. 2012. "A neural circuit for spatial summation in visual cortex." *Nature* (Nature Publishing Group) 490: 226–231.

Ahmadian, Yashar, Daniel B. Rubin, and Kenneth D. Miller. 2013. "Analysis of the stabilized supralinear network." *Neural computation* (MIT Press) 25: 1994–2037.

Anderson, Jeffrey S., Ilan Lampl, Deda C. Gillespie, and David Ferster. 2000. "The contribution of noise to contrast invariance of orientation tuning in cat visual cortex." *Science* (American Association for the Advancement of Science) 290: 1968–1972.

Angelucci, Alessandra, Maryam Bijanzadeh, Lauri Nurminen, Frederick Federer, Sam Merlin, and Paul C. Bressloff. 2017. "Circuits and mechanisms for surround modulation in visual cortex." *Annual review of neuroscience* (Annual Reviews) 40: 425–451.

Atallah, Bassam V., William Bruns, Matteo Carandini, and Massimo Scanziani. 2012. "Parvalbumin-expressing interneurons linearly transform cortical responses to visual stimuli." *Neuron* (Elsevier) 73: 159–170.

913 Cavanaugh, James R., Wyeth Bair, and J. Anthony Movshon. 2002. "Nature and interaction of
914 signals from the receptive field center and surround in macaque V1 neurons." *Journal of*
915 *neurophysiology* (American Physiological Society Bethesda, MD) 88: 2530–2546.
916 Chen, Gang, Yang Dan, and Chao-Yi Li. 2005. "Stimulation of non-classical receptive field
917 enhances orientation selectivity in the cat." *The Journal of physiology* (Wiley Online
918 Library) 564: 233–243.
919 Coen-Cagli, Ruben, Adam Kohn, and Odelia Schwartz. 2015. "Flexible gating of contextual
920 influences in natural vision." *Nature neuroscience* (Nature Publishing Group) 18: 1648–
921 1655.
922 Del Molino, Luis Carlos Garcia, Guangyu Robert Yang, Jorge F. Mejias, and Xiao-Jing Wang.
923 2017. "Paradoxical response reversal of top-down modulation in cortical circuits with
924 three interneuron types." *Elife* (eLife Sciences Publications Limited) 6: e29742.
925 Dipoppa, Mario, Adam Ranson, Michael Krumin, Marius Pachitariu, Matteo Carandini, and
926 Kenneth D. Harris. 2018. "Vision and locomotion shape the interactions between neuron
927 types in mouse visual cortex." *Neuron* (Elsevier) 98: 602–615.
928 Douglas, Rodney J., Christof Koch, Misha Mahowald, K. A. Martin, and Humbert H. Suarez. 1995.
929 "Recurrent excitation in neocortical circuits." *Science* (American Association for the
930 Advancement of Science) 269: 981–985.
931 Dudai, Amir, Nadav Yayon, Vitaly Lerner, Gen-ichi Tasaka, Yair Deitcher, Karin Gorfine, Naomi
932 Niederhoffer, Adi Mizrahi, Hermona Soreq, and Michael London. 2020. "Barrel cortex
933 VIP/ChAT interneurons suppress sensory responses in vivo." *PLoS biology* (Public Library
934 of Science San Francisco, CA USA) 18: e3000613.
935 Fu, Yu, Jason M. Tucciarone, J. Sebastian Espinosa, Nengyin Sheng, Daniel P. Darcy, Roger A.
936 Nicoll, Z. Josh Huang, and Michael P. Stryker. 2014. "A cortical circuit for gain control by
937 behavioral state." *Cell* (Elsevier) 156: 1139–1152.
938 Hakim, Richard, Kiarash Shamardani, and Hillel Adesnik. 2018. "A neural circuit for gamma-band
939 coherence across the retinotopic map in mouse visual cortex." *Elife* (eLife Sciences
940 Publications Limited) 7: e28569.
941 Hawken, Michael J., Robert M. Shapley, Michael P. Sceniak, Dario L. Ringach, and Elizabeth N.
942 Johnson. 2001. "Contrast gain, area summation and temporal tuning in primate visual
943 cortex." In *Vision and attention*, 41–62. Springer.
944 He, Miao, Jason Tucciarone, SooHyun Lee, Maximiliano José Nigro, Yongsoo Kim, Jesse Maurica
945 Levine, Sean Michael Kelly, et al. 2016. "Strategies and tools for combinatorial targeting
946 of GABAergic neurons in mouse cerebral cortex." *Neuron* (Elsevier) 91: 1228–1243.
947 Kamigaki, Tsukasa, and Yang Dan. 2017. "Delay activity of specific prefrontal interneuron
948 subtypes modulates memory-guided behavior." *Nature neuroscience* (Nature Publishing
949 Group) 20: 854.
950 Kapadia, Mitesh K., Gerald Westheimer, and Charles D. Gilbert. 1999. "Dynamics of spatial
951 summation in primary visual cortex of alert monkeys." *Proceedings of the National*
952 *Academy of Sciences* (National Acad Sciences) 96: 12073–12078.
953 Kapfer, Christoph, Lindsey L. Glickfeld, Bassam V. Atallah, and Massimo Scanziani. 2007.
954 "Supralinear increase of recurrent inhibition during sparse activity in the somatosensory
955 cortex." *Nature neuroscience* (Nature Publishing Group) 10: 743–753.

Karnani, Mahesh M., Jesse Jackson, Inbal Ayzenshtat, Jason Tucciarone, Kasra Manoocheri, William G. Snider, and Rafael Yuste. 2016. "Cooperative subnetworks of molecularly similar interneurons in mouse neocortex." *Neuron* (Elsevier) 90: 86–100.

Kato, Hiroyuki K., Samuel K. Asinof, and Jeffry S. Isaacson. 2017. "Network-level control of frequency tuning in auditory cortex." *Neuron* (Elsevier) 95: 412–423.

Keller, Andreas J., Morgane M. Roth, Matthew Caudill, Mario Dipoppa, Kenneth D. Miller, and Massimo Scanziani. 2020. "A disinhibitory circuit for contextual modulation in primary visual cortex." *bioRxiv* (Cold Spring Harbor Laboratory).

Kuchibhotla, Kishore V., Jonathan V. Gill, Grace W. Lindsay, Eleni S. Papadoyannis, Rachel E. Field, Tom A. Hindmarsh Sten, Kenneth D. Miller, and Robert C. Froemke. 2017. "Parallel processing by cortical inhibition enables context-dependent behavior." *Nature neuroscience* (Nature Publishing Group) 20: 62–71.

Lee, Seung-Hee, Alex C. Kwan, and Yang Dan. 2014. "Interneuron subtypes and orientation tuning." *Nature* (Nature Publishing Group) 508: E1–E2.

Lee, Seung-Hee, Alex C. Kwan, Siyu Zhang, Victoria Phoumthipphavong, John G. Flannery, Sotiris C. Masmanidis, Hiroki Taniguchi, et al. 2012. "Activation of specific interneurons improves V1 feature selectivity and visual perception." *Nature* (Nature Publishing Group) 488: 379–383.

Lee, Soohyun, Illya Kruglikov, Z. Josh Huang, Gord Fishell, and Bernardo Rudy. 2013. "A disinhibitory circuit mediates motor integration in the somatosensory cortex." *Nature neuroscience* (Nature Publishing Group) 16: 1662–1670.

Letzkus, Johannes J., Steffen B. E. Wolff, Elisabeth M. M. Meyer, Philip Tovote, Julien Courtin, Cyril Herry, and Andreas Lüthi. 2011. "A disinhibitory microcircuit for associative fear learning in the auditory cortex." *Nature* (Nature Publishing Group) 480: 331–335.

Levitt, Jonathan B., and Jennifer S. Lund. 1997. "Contrast dependence of contextual effects in primate visual cortex." *Nature* (Nature Publishing Group) 387: 73–76.

Li, Ling-yun, Xiaorui R. Xiong, Leena A. Ibrahim, Wei Yuan, Huizhong W. Tao, and Li I. Zhang. 2015. "Differential receptive field properties of parvalbumin and somatostatin inhibitory neurons in mouse auditory cortex." *Cerebral cortex* (Oxford University Press) 25: 1782–1791.

Li, Ling-yun, Ya-tang Li, Mu Zhou, Huizhong W. Tao, and Li I. Zhang. 2013. "Intracortical multiplication of thalamocortical signals in mouse auditory cortex." *Nature neuroscience* (Nature Publishing Group) 16: 1179–1181.

Li, Ya-tang, Leena A. Ibrahim, Bao-hua Liu, Li I. Zhang, and Huizhong Whit Tao. 2013. "Linear transformation of thalamocortical input by intracortical excitation." *Nature neuroscience* (Nature Publishing Group) 16: 1324–1330.

Lien, Anthony D., and Massimo Scanziani. 2013. "Tuned thalamic excitation is amplified by visual cortical circuits." *Nature neuroscience* (Nature Publishing Group) 16: 1315–1323.

Litwin-Kumar, Ashok, Robert Rosenbaum, and Brent Doiron. 2016. "Inhibitory stabilization and visual coding in cortical circuits with multiple interneuron subtypes." *Journal of neurophysiology* (American Physiological Society Bethesda, MD) 115: 1399–1409.

Mesik, Lukas, Wen-pei Ma, Ling-yun Li, Leena A. Ibrahim, Z. J. Huang, Li I. Zhang, and Huizhong W. Tao. 2015. "Functional response properties of VIP-expressing inhibitory neurons in mouse visual and auditory cortex." *Frontiers in neural circuits* (Frontiers) 9: 22.

Miller, Kenneth D., and Todd W. Troyer. 2002. "Neural noise can explain expansive, power-law nonlinearities in neural response functions." *Journal of neurophysiology* (American Physiological Society Bethesda, MD) 87: 653–659.

Millman, Daniel J., Gabriel Koch Ocker, Shiella Caldejon, Josh D. Larkin, Eric Kenji Lee, Jennifer Luviano, Chelsea Nayan, et al. 2019. "VIP interneurons selectively enhance weak but behaviorally-relevant stimuli." *bioRxiv* (Cold Spring Harbor Laboratory) 858001.

Mineault, Patrick J., Elaine Tring, Joshua T. Trachtenberg, and Dario L. Ringach. 2016. "Enhanced spatial resolution during locomotion and heightened attention in mouse primary visual cortex." *Journal of Neuroscience* (Soc Neuroscience) 36: 6382–6392.

Nauhaus, Ian, Laura Busse, Matteo Carandini, and Dario L. Ringach. 2009. "Stimulus contrast modulates functional connectivity in visual cortex." *Nature neuroscience* (Nature Publishing Group) 12: 70.

Nienborg, Hendrikje, Andrea Hasenstaub, Ian Nauhaus, Hiroki Taniguchi, Z. Josh Huang, and Edward M. Callaway. 2013. "Contrast dependence and differential contributions from somatostatin-and parvalbumin-expressing neurons to spatial integration in mouse V1." *Journal of Neuroscience* (Soc Neuroscience) 33: 11145–11154.

Okamoto, Masahiro, Tomoyuki Naito, Osamu Sadakane, Hironobu Osaki, and Hiromichi Sato. 2009. "Surround suppression sharpens orientation tuning in the cat primary visual cortex." *European Journal of Neuroscience* (Wiley Online Library) 29: 1035–1046.

Orban, G. A., H. Kato, and P. O. Bishop. 1979. "End-zone region in receptive fields of hypercomplex and other striate neurons in the cat." *Journal of Neurophysiology* (American Physiological Society Bethesda, MD) 42: 818–832.

Ozeki, Hirofumi, Ian M. Finn, Evan S. Schaffer, Kenneth D. Miller, and David Ferster. 2009. "Inhibitory stabilization of the cortical network underlies visual surround suppression." *Neuron* (Elsevier) 62: 578–592.

Pfeffer, Carsten K., Mingshan Xue, Miao He, Z. Josh Huang, and Massimo Scanziani. 2013. "Inhibition of inhibition in visual cortex: the logic of connections between molecularly distinct interneurons." *Nature neuroscience* (Nature Publishing Group) 16: 1068–1076.

Phillips, Elizabeth A. K., and Andrea R. Hasenstaub. 2016. "Asymmetric effects of activating and inactivating cortical interneurons." *Elife* (eLife Sciences Publications Limited) 5: e18383.

Pi, Hyun-Jae, Balázs Hangya, Duda Kvitsiani, Joshua I. Sanders, Z. Josh Huang, and Adam Kepecs. 2013. "Cortical interneurons that specialize in disinhibitory control." *Nature* (Nature Publishing Group) 503: 521–524.

Polat, Uri, Keiko Mizobe, Mark W. Pettet, Takuji Kasamatsu, and Anthony M. Norcia. 1998. "Collinear stimuli regulate visual responses depending on cell's contrast threshold." *Nature* (Nature Publishing Group) 391: 580–584.

Reinhold, Kimberly, Anthony D. Lien, and Massimo Scanziani. 2015. "Distinct recurrent versus afferent dynamics in cortical visual processing." *Nature neuroscience* (Nature Publishing Group) 18: 1789–1797.

Rubin, Daniel B., Stephen D. Van Hooser, and Kenneth D. Miller. 2015. "The stabilized supralinear network: a unifying circuit motif underlying multi-input integration in sensory cortex." *Neuron* (Elsevier) 85: 402–417.

1042 Rudy, Bernardo, Gordon Fishell, SooHyun Lee, and Jens Hjerling-Leffler. 2011. "Three groups of
1043 interneurons account for nearly 100% of neocortical GABAergic neurons."
1044 *Developmental neurobiology* (Wiley Online Library) 71: 45–61.
1045 Sanzeni, Alessandro, Bradley Akitake, Hannah C. Goldbach, Caitlin E. Leedy, Nicolas Brunel, and
1046 Mark H. Histed. 2020. "Inhibition stabilization is a widespread property of cortical
1047 networks." *Elife* (eLife Sciences Publications Limited) 9: e54875.
1048 Sato, Tatsuo K., Michael Häusser, and Matteo Carandini. 2014. "Distal connectivity causes
1049 summation and division across mouse visual cortex." *Nature neuroscience* (Nature
1050 Publishing Group) 17: 30–32.
1051 Sceniak, Michael P., Dario L. Ringach, Michael J. Hawken, and Robert Shapley. 1999. "Contrast's
1052 effect on spatial summation by macaque V1 neurons." *Nature neuroscience* (Nature
1053 Publishing Group) 2: 733–739.
1054 Schwabe, Lars, Jennifer M. Ichida, S. Shushruth, Pradeep Mangapathy, and Alessandra
1055 Angelucci. 2010. "Contrast-dependence of surround suppression in Macaque V1:
1056 experimental testing of a recurrent network model." *Neuroimage* (Elsevier) 52: 777–
1057 792.
1058 Sengpiel, Frank, Arjune Sen, and Colin Blakemore. 1997. "Characteristics of surround inhibition
1059 in cat area 17." *Experimental brain research* (Springer) 116: 216–228.
1060 Tasic, Bosiljka, Zizhen Yao, Lucas T. Graybuck, Kimberly A. Smith, Thuc Nghi Nguyen, Darren
1061 Bertagnolli, Jeff Goldy, et al. 2018. "Shared and distinct transcriptomic cell types across
1062 neocortical areas." *Nature* (Nature Publishing Group) 563: 72–78.
1063 Tosches, Maria Antonietta, Tracy M. Yamawaki, Robert K. Naumann, Ariel A. Jacobi, Georgi
1064 Tushev, and Gilles Laurent. 2018. "Evolution of pallium, hippocampus, and cortical cell
1065 types revealed by single-cell transcriptomics in reptiles." *Science* (American Association
1066 for the Advancement of Science) 360: 881–888.
1067 Toth, Louis J., S. Chenchal Rao, Dae-Shik Kim, David Somers, and Mriganka Sur. 1996.
1068 "Subthreshold facilitation and suppression in primary visual cortex revealed by intrinsic
1069 signal imaging." *Proceedings of the National Academy of Sciences* (National Acad
1070 Sciences) 93: 9869–9874.
1071 Tsodyks, Misha V., William E. Skaggs, Terrence J. Sejnowski, and Bruce L. McNaughton. 1997.
1072 "Paradoxical effects of external modulation of inhibitory interneurons." *Journal of*
1073 *neuroscience* (Soc Neuroscience) 17: 4382–4388.
1074 Vaiceliunaite, Agne, Sinem Erisken, Florian Franzen, Steffen Katzner, and Laura Busse. 2013.
1075 "Spatial integration in mouse primary visual cortex." *Journal of neurophysiology*
1076 (American Physiological Society Bethesda, MD) 110: 964–972.
1077 Wang, Xiao-Jing, and Guangyu Robert Yang. 2018. "A disinhibitory circuit motif and flexible
1078 information routing in the brain." *Current opinion in neurobiology* (Elsevier) 49: 75–83.
1079 Wilson, Nathan R., Caroline A. Runyan, Forea L. Wang, and Mriganka Sur. 2012. "Division and
1080 subtraction by distinct cortical inhibitory networks in vivo." *Nature* (Nature Publishing
1081 Group) 488: 343–348.
1082 Xing, Dajun, Robert M. Shapley, Michael J. Hawken, and Dario L. Ringach. 2005. "Effect of
1083 stimulus size on the dynamics of orientation selectivity in Macaque V1." *Journal of*
1084 *Neurophysiology* (American Physiological Society) 94: 799–812.

Yang, Guangyu Robert, John D. Murray, and Xiao-Jing Wang. 2016. "A dendritic disinhibitory circuit mechanism for pathway-specific gating." *Nature communications* (Nature Publishing Group) 7: 1–14.

Zhang, Siyu, Min Xu, Tsukasa Kamigaki, Johnny Phong Hoang Do, Wei-Cheng Chang, Sean Jenvay, Kazunari Miyamichi, Liqun Luo, and Yang Dan. 2014. "Long-range and local circuits for top-down modulation of visual cortex processing." *Science* (American Association for the Advancement of Science) 345: 660–665.